

1 SEARCH FOR PRODUCTION OF A HIGGS BOSON AND A SINGLE TOP
2 QUARK IN MULTILEPTON FINAL STATES IN pp COLLISIONS AT $\sqrt{s} = 13$
3 TeV.

4 by

5 Jose Andres Monroy Montañez

A DISSERTATION

7 Presented to the Faculty of

8 The Graduate College at the University of Nebraska

In Partial Fulfilment of Requirements

10 For the Degree of Doctor of Philosophy

11 Major: Physics and Astronomy

¹² Under the Supervision of Kenneth Bloom and Aaron Dominguez

13 Lincoln, Nebraska

14 July, 2018

15 SEARCH FOR PRODUCTION OF A HIGGS BOSON AND A SINGLE TOP
16 QUARK IN MULTILEPTON FINAL STATES IN pp COLLISIONS AT $\sqrt{s} = 13$
17 TeV.

18 Jose Andres Monroy Montañez, Ph.D.

19 University of Nebraska, 2018

20 Adviser: Kenneth Bloom and Aaron Dominguez

²¹ Table of Contents

²² Table of Contents	iii
²³ List of Figures	vii
²⁴ List of Tables	ix
²⁵ 1 INTRODUCTION	1
²⁶ 2 Theoretical approach	2
27 2.1 Introduction	2
28 2.2 Standard model of particle physics	3
29 2.2.1 Fermions	5
30 2.2.1.1 Leptons	6
31 2.2.1.2 Quarks	8
32 2.2.2 Fundamental interactions	12
33 2.2.3 Gauge Bosons	18
34 2.3 Electroweak unification and the Higgs mechanism	20
35 2.3.1 Spontaneous symmetry breaking	27
36 2.3.2 Higgs mechanism	31
37 2.3.3 Masses of the gauge bosons	34

38	2.3.4	Masses of the fermions	35
39	2.3.5	The Higgs field	36
40	2.3.6	Higgs boson production mechanisms at LHC.	37
41	2.3.7	Higgs decay channels	41
42	2.4	Associated Production of Higgs Boson and Single Top Quark.	42
43	2.5	The CP-mixing in tH processes	46
44	3	The CMS experiment at the LHC	51
45	3.1	Introduction	51
46	3.2	The LHC	52
47	3.3	The CMS experiment	56
48	3.3.1	coordinate system	58
49	3.3.2	tracker- pixels and strips	58
50	3.3.3	calorimeters	58
51	3.3.4	magnet	58
52	3.3.5	muon system	58
53	3.3.6	trigger system - HLT- L1	58
54	3.3.7	computing model	58
55	3.4	Event generation simulation and reconstruction	58
56	3.4.1	event generation	58
57	3.4.2	Hard scattering	58
58	3.4.3	parton shower	58
59	3.4.4	hadronization and decays	58
60	3.4.5	underlying events and pileup	58
61	3.4.6	MC - MadEvent, MadGraph and madgraphNLO, powheg, pythia, tauola	58

63	3.4.7	detector simulation	58
64	3.4.8	event reconstruction- particle flow algorithm, vertexing , muon	
65		reco, electron reco, photon and hadron reco, jets reco, anti-kt	
66		algoritm, jet energy corrections, btagging, MET	58
67	3.4.9	MVA methods, NN, BDT, boosting, overtraining, variable	
68		ranking	58
69	3.4.10	statistical inference, likelihood parametrization	58
70	3.4.11	nuisance paraeters	58
71	3.4.12	exclusion limits	58
72	3.4.13	asymptotic limits	58
73	4	Search for production of a Higgs boson and a single top quark in	
74	multilepton final states in pp collisions at $\sqrt{s} = 13$ TeV		59
75	4.1	Introduction	59
76	4.2	Data and MC Samples	61
77	4.2.1	Full 2016 dataset and MC samples	61
78	4.2.2	Triggers	64
79	4.2.2.1	Trigger efficiency scale factors	64
80	4.3	Object Identification and event selection	65
81	4.3.1	Jets and b tagging	65
82	4.3.2	Lepton selection	66
83	4.3.3	Lepton selection efficiency	67
84	4.4	Background predictions	68
85	4.5	Signal discrimination	69
86	4.5.1	Classifiers response	73
87	4.6	Additional discriminating variables	76

88	5 The CMS forward pixel detector	79
89	5.0.1 The phase 1 FPix upgrade	79
90	5.0.2 FPix module production line	79
91	5.0.3 The Gluing stage	79
92	5.0.4 The Encapsulation stage	79
93	5.0.5 The FPix module production yields	79
94	Bibliography	79
95	References	80

⁹⁶ List of Figures

97	1.1	^{14}N neutron capture in a PECVD polymerized pyridine film. The Q-value of this reaction is 626 keV. Taken from [22]	1
99	2.1	Standard model of particle physics.	4
100	2.2	WI transformations between quarks	12
101	2.3	Fundamental interactions in nature.	13
102	2.4	SM interactions diagrams	14
103	2.5	Neutral current processes	21
104	2.6	Spontaneous symmetry breaking mechanism	28
105	2.7	SSB Potential form	29
106	2.8	Potential for complex scalar field	30
107	2.9	SSB mechanism for complex scalar field	31
108	2.10	Proton-Proton collision	38
109	2.11	Higgs production mechanism Feynman diagrams	39
110	2.12	Higgs production cross section and decay branching ratios	39
111	2.13	Associated Higgs production mechanism Feynman diagrams	42
112	2.14	Cross section for tHq process as a function of C_t	45
113	2.15	Cross section for tHW process as a function of κ_{Htt}	46
114	2.16	NLO cross section for tX_0 and $t\bar{t}X_0$	49

115	2.17 NLO cross section for tWX_0 , $t\bar{t}X_0$ and $tWX_0 + t\bar{t}X_0 + \text{interference}$	50
116	3.1 Layout of the LEP tunnel including LHC infrastructure additions	52
117	3.2 ref. C.Lefevre, “The CERN accelerator complex,” (2008). CERN-DI-	
118	0812015.	54
119	3.3 ref. ACTeam, “Diagram of an LHC dipole magnet. Schéma d’un aimant	
120	dipôle du LHC,” (1999). CERN-DI-9906025.	55
121	3.4 ref: CMS Collaboration, “Detector Drawings”, CMS-PHO-GEN-2012-002,	
122	http://cds.cern.ch/record/1433717 , 2012.	57
123	4.1 The two leading-order diagrams of tHq production.	60
124	4.2 Input variables to the BDT for signal discrimination normalized.	70
125	4.3 Input variables to the BDT for signal discrimination not normalized. . .	72
126	4.4 BDT inputs as seen by TMVA against $t\bar{t}$	73
127	4.5 BDT inputs as seen by TMVA against $t\bar{t}V$	74
128	4.6 Correlation matrices for the input variables in the TMVA.	75
129	4.7 MVA classifiers performance.	75
130	4.8 Additional discriminating variables distributions.	77

¹³¹ List of Tables

132	2.1	Fermions of the SM.	5
133	2.2	Fermion masses.	6
134	2.3	Leptons properties.	9
135	2.4	Quarks properties.	9
136	2.5	Fermion weak isospin and weak hypercharge multiplets.	11
137	2.6	Fundamental interactions features.	15
138	2.7	SM gauge bosons.	19
139	2.8	Higgs boson properties.	37
140	2.9	Predicted branching ratios for a SM Higgs boson with $m_H = 125 \text{ GeV}/c^2$	41
141	2.10	Predicted SM cross sections for tH production at $\sqrt{s} = 13 \text{ TeV}$	43
142	2.11	Predicted enhancement of the tHq and tHW cross sections at LHC	47
143	4.1	Signal samples and their cross section and branching fraction.	61
144	4.2	κ_V and κ_t combinations.	62
145	4.3	List of background samples used in this analysis (CMSSW 80X).	63
146	4.4	Leading-order $t\bar{t}W$ and $t\bar{t}Z$ samples used in the signal BDT training. . . .	63
147	4.5	Table of high-level triggers that we consider in the analysis.	64
148	4.6	Trigger efficiency scale factors and associated uncertainties.	65
149	4.7	Requirements on each of the three muon selections.	66

150	4.8	Criteria for each of the three electron selections.	67
151	4.9	MVA input discriminating variables	71
152	4.10	TMVA input variables ranking for BDTA_GRAD method	76
153	4.11	TMVA configuration used in the BDT training.	76
154	4.12	ROC-integral for all the testing cases.	78

¹⁵⁵ Chapter 1

¹⁵⁶ INTRODUCTION

Figure 1.1: ^{14}N neutron capture in a PECVD polymerized pyridine film. The Q-value of this reaction is 626 keV. Taken from [22]

¹⁵⁷ **Chapter 2**

¹⁵⁸ **Theoretical approach**

¹⁵⁹ **2.1 Introduction**

¹⁶⁰ The physical description of the universe is a challenge that physicists have faced by
¹⁶¹ making theories that refine existing principles and proposing new ones in an attempt
¹⁶² to embrace emerging facts and phenomena.

¹⁶³ At the end of 1940s Julian Schwinger [11] and Richard P. Feynman [12], based in
¹⁶⁴ the work of Sin-Itiro Tomonaga [13], developed an electromagnetic theory consistent
¹⁶⁵ with special relativity and quantum mechanics that describes how matter and light
¹⁶⁶ interact; the so-called “quantum eletrodynamics” (QED) had born.

¹⁶⁷

¹⁶⁸ QED has become the guide in the development of theories that describe the universe.
¹⁶⁹ It was the first example of a quantum field theory (QFT), which is the theoretical
¹⁷⁰ framework for building quantum mechanical models that describes particles and their
¹⁷¹ interactions. QFT is composed of a set of mathematical tools that combines classical
¹⁷² fields, special relativity, and quantum mechanics while keeping the quantum point
¹⁷³ particles and locality ideas.

174 This chapter gives an overview of the standard model of particle physics, starting
 175 with a description of the particles and interactions that compose it, followed by a
 176 description of the electroweak interaction, the Higgs boson and the associated pro-
 177 duction of Higgs boson and a single top quark (tH). The description contained in
 178 this chapter is based on references [1–3].

179 2.2 Standard model of particle physics

180 Particle physics at the fundamental level is modeled in terms of a collection of in-
 181 teracting particles and fields in a theory known as the “standard model of particle
 182 physics (SM)”¹.

183 The full picture of the SM is composed of three fields², whose excitations are inter-
 184 preted as particles called mediators or force-carriers; a set of fields, whose excitations
 185 are interpreted as elementary particles, interacting through the exchange of those
 186 mediators and a field that give the mass to elementary particles. Figure 2.1 shows an
 187 scheme of the SM particles organization. In addition to the particles in the scheme
 188 (but not listed in it), their corresponding anti-particles, with opposite quantum num-
 189 bers, are also part of the picture; some particles are their own anti-particles, like
 190 photon or Higgs, or anti-particle is already listed like in the W^+ and W^- case.

191

192 The mathematical formulation of the SM is based on group theory and the use of
 193 Noether’s theorem [17] which states that for a physical system modeled by a La-
 194 grangian that is invariant under a group of transformations a conservation law is

¹ The formal and complete treatment of the SM is out of the scope of this document, however a plenty of textbooks describing it at several levels are available in the literature. The treatment in “An Introduction To Quantum Field Theory (Frontiers in Physics)” by Michael E. Peskin and Dan V. Schroeder is quite comprehensive and detailed.

² Note that gravitational field is not included in the standard model formulation

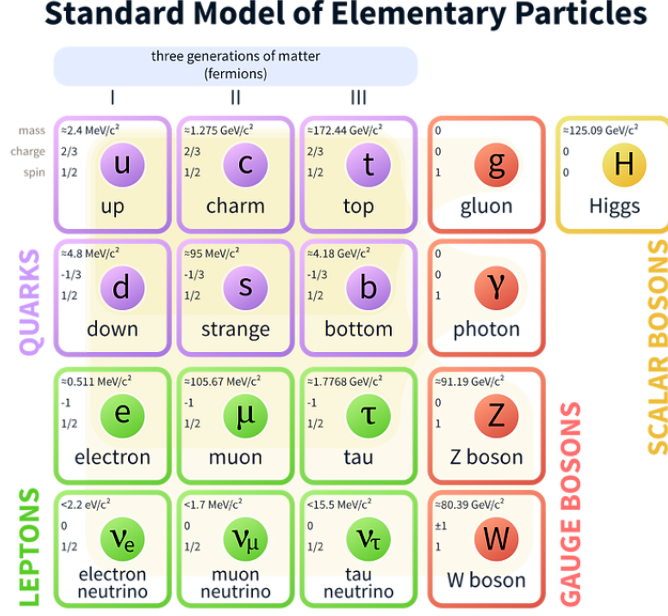


Figure 2.1: Schematic representation of the Standard model of particle physics. SM is a theoretical model intended to describe three of the four fundamental forces of the universe in terms of a set of particles and their interactions. [18].

195 expected. For instance, a system described by a time-independent Lagrangian is
 196 invariant (symmetric) under time changes (transformations) with the total energy
 197 conservation law as the expected conservation law. In QED, the charge operator
 198 (Q) is the generator of the $U(1)$ symmetry which according to the Noether's theorem
 199 means that there is a conserved quantity; this conserved quantity is the electric charge
 200 and thus the law conservation of electric charge is established.

201

202 In the SM, the symmetry group $SU(3)_C \otimes SU(2)_L \otimes U(1)_Y$ describes three of the
 203 four fundamental interactions in nature(see section 2.2.2): strong interaction(SI),
 204 weak interaction(WI) and electromagnetic interactions (EI) in terms of symmetries
 205 associated to physical quantities:

206 • Strong: $SU(3)_C$ associated to color charge

- 207 • Weak: $SU(2)_L$ associated to weak isospin and chirality
 208 • Electromagnetic: $U(1)_Y$ associated to weak hypercharge and electric charge

209 It will be shown that the electromagnetic and weak interactions are combined in
 210 the so-called electroweak interaction where chirality, hypercharge, weak isospin and
 211 electric charge are the central concepts.

212 **2.2.1 Fermions**

213 The basic constituents of the ordinary matter at the lowest level, which form the set
 214 of elementary particles in the SM formulation, are quarks and leptons. All of them
 215 have spin 1/2, therefore they are classified as fermions since they obey Fermi-Dirac
 216 statistics. There are six “flavors” of quarks and three of leptons organized in three
 217 generations, or families, as shown in table 2.1.

218

		Generation		
Type		1st	2nd	3rd
Leptons	Charged	Electron (e)	Moun(μ)	Tau (τ)
	Neutral	Electron neutrino (ν_e)	Muon neutrino (ν_μ)	Tau neutrino (ν_τ)
Quarks	Up-type	Up (u)	Charm (c)	Top (t)
	Down-type	Down (d)	Strange (s)	Bottom (b)

Table 2.1: Fermions of the SM. There are six flavors of quarks and three of leptons, organized in three generations, or families, composed of two pairs of closely related particles. The close relationship is motivated by the fact that WI between leptons is limited to the members of the same generation; WI between quarks is not limited but greatly favoured, to same generation members.

219

220 There is a mass hierarchy between generations (see table 2.2), where the higher gener-
 221 ation particles decays to the lower one, which can explain why the ordinary matter is

made of particles in the first generation. In the SM, neutrinos are modeled as massless particles so they are not subject to this mass hierarchy; however, today it is known that neutrinos are massive so the hierarchy could be restated. The reason behind this mass hierarchy is one of the most important open questions in particle physics, and it becomes more puzzling when noticing that the mass difference between first and second generation fermions is small compared to the mass difference with respect to the third generation.

Lepton	Mass (MeV/c ²)	Quark	Mass (MeV/c ²)
e	0.51	u	2.2
μ	105.65	c	1.28×10^3
τ	1776.86	t	173.1×10^3
ν_e	Unknown	d	4.7
ν_μ	Unknown	s	96
τ_μ	Unknown	b	4.18×10^3

Table 2.2: Fermion masses [21]. Generations differ by mass in a way that have been interpreted as a masss hierarchy. Approximate values with no uncertainties are used, for comparison purpose.

229

Usually, the second and third generation fermions are produced in high energy processes, like the ones recreated in the particle accelerators.

232 2.2.1.1 Leptons

A lepton is an elementary particle that is not subject to the SI. As seen in table 2.1, there are two types of leptons, the charged ones (electron, muon and tau) and the neutral ones (the three neutrinos). The electric charge (Q) is the property that gives leptons the ability to participate in the EI. From the classical point of view, Q plays a central role determining, among others, the strength of the electric field through which the electromagnetic force is exerted. It is clear that neutrinos are not affected

239 by EI because they don't carry electric charge.

240

241 Another feature of the leptons that is fundamental in the mathematical description
 242 of the SM is the chirality, which is closely related to spin and helicity. Helicity de-
 243 fine the handedness of a particle by relating its spin and momentum such that if
 244 they are parallel then the particle is right-handed; if spin and momentum are an-
 245 tiparallel the particle is said to be left-handed. The study of parity conservation (or
 246 violation) in β -decay have shown that only left-handed electrons/neutrinos or right-
 247 handed positrons/anti-neutrinos are created [19]; the inclusion of that feature in the
 248 theory was achieved by using projection operators for helicity, however, helicity is
 249 frame dependent for massive particles which makes it not Lorentz invariant and then
 250 another related attribute has to be used: *chirality*.

251

252 Chirality is a purely quantum attribute which makes it not so easy to describe in
 253 graphical terms but it defines how the wave function of a particle transforms under
 254 certain rotations. As with helicity, there are two chiral states, left-handed chiral
 255 (L) and right-handed chiral (R). In the highly relativistic limit where $E \approx p \gg m$
 256 helicity and chirality converge, becoming exactly the same for massless particles. In
 257 the following when referring to left-handed (right-handed) it means left-handed chiral
 258 (right-handed chiral). The fundamental fact about chirality is that while EI and SI
 259 are not sensitive to chirality, in WI left-handed and right-handed fermions are treated
 260 asymmetrically, such that only left handed fermions and right-handed anti-fermions
 261 are allowed to couple to WI mediators, which is a violation of parity. The way to
 262 translate this statement in a formal mathematical formulation is based on the isospin
 263 symmetry group $SU(2)_L$.

264 Each generation of leptons is seen as a weak isospin doublet.³ The left-handed charged
 265 lepton and its associated left-handed neutrino are arranged in doublets of weak isospin
 266 T=1/2 while their right-handed partners are singlets:

$$\begin{pmatrix} \nu_l \\ l \end{pmatrix}_L, l_R := \begin{pmatrix} \nu_e \\ e \end{pmatrix}_L, \begin{pmatrix} \nu_\mu \\ \mu \end{pmatrix}_L, \begin{pmatrix} \nu_\tau \\ \tau \end{pmatrix}_L, e_R, \mu_R, \tau_R, \nu_{eR}, \nu_{\mu R}, \nu_{\tau R} \quad (2.1)$$

267 The isospin third component refers to the eigenvalues of the weak isospin operator
 268 which for doublets is $T_3 = \pm 1/2$, while for singlets it is $T_3 = 0$. The physical meaning
 269 of this doublet-singlet arrangement falls in that the WI couples the two particles in
 270 the doublet by exchanging the interaction mediator while the singlet member is not
 271 involved in WI. The main properties of the leptons are summarized in table 2.3.

272

273 Altough all three flavor neutrinos have been observed, their masses remain unknown
 274 and only some estimations have been made [20]. The main reason is that the fla-
 275 vor eigenstates are not the same as the mass eigenstates which imply that when a
 276 neutrino is created its mass state is a linear combination of the three mass eigen-
 277 states and experiments can only probe the squared difference of the masses. The
 278 Pontecorvo-Maki-Nakagawa-Sakata (PMNS) mixing matrix encode the relationship
 279 between flavor and mass eigenstates.

280

281 2.2.1.2 Quarks

282 Quarks are the basic constituents of protons and neutrons. The way quarks join to
 283 form bound states, called “hadrons”, is through the SI. Quarks are affected by all the

³ The weak isospin is an analogy of the isospin symmetry in strong interaction where neutron and proton are affected equally by strong force but differ in their charge.

Lepton	Q(e)	T_3	L_e	L_μ	L_τ	Lifetime (s)
Electron (e)	-1	-1/2	1	0	0	Stable
Electron neutrino(ν_e)	0	1/2	1	0	0	Unknown
Muon (μ)	-1	-1/2	0	1	0	2.19×10^{-6}
Muon neutrino (ν_μ)	0	1/2	0	1	0	Unknown
Tau (τ)	-1	-1/2	0	0	1	290.3×10^{-15}
Tau neutrino (τ_μ)	0	1/2	0	0	1	Unknown

Table 2.3: Leptons properties [21]. Q: electric charge, T_3 : weak isospin. Only left-handed leptons and right-handed anti-leptons participate in the WI. Anti-particles with inverted T_3 , Q and lepton number complete the leptons set but are not listed. Right-handed leptons and left-handed anti-leptons, neither listed, form weak isospin singlets with $T_3 = 0$ and do not take part in the weak interaction.

284 fundamental interactions which means that they carry all the four types of charges:
285 color, electric charge, weak isospin and mass.

Flavor	Q(e)	I_3	T_3	B	C	S	T	B'	Y	Color
Up (u)	2/3	1/2	1/2	1/3	0	0	0	0	1/3	r,b,g
Charm (c)	2/3	0	1/2	1/3	1	0	0	0	4/3	r,b,g
Top(t)	2/3	0	1/2	1/3	0	0	1	0	4/3	r,b,g
Down(d)	-1/3	-1/2	-1/2	1/3	0	0	0	0	1/3	r,b,g
Strange(s)	-1/3	0	-1/2	1/3	0	-1	0	0	-2/3	r,b,g
Bottom(b)	-1/3	0	-1/2	1/3	0	0	0	-1	-2/3	r,b,g

Table 2.4: Quarks properties [21]. Q: electric charge, I_3 : isospin, T_3 : weak isospin, B: baryon number, C: charmness, S: strangeness, T: topness, B' : bottomness, Y: hypercharge. Anti-quarks posses the same mass and spin as quarks but all charges (color, flavor numbers) have opposite sign.

286

287 Table 2.4 summarizes the features of quarks, among which the most particular is
288 their fractional electric charge. Note that fractional charge is not a problem, given
289 that quarks are not found isolated, but serves to explain how composed particles are
290 formed out of two or more valence quarks⁴.

291

⁴ Hadrons can contain an indefinite number of virtual quarks and gluons, known as the quark and gluon sea, but only the valence quarks determine hadrons' quantum numbers.

292 Color charge is the responsible for the SI between quarks and is the symmetry
 293 ($SU(3)_C$) that defines the formalism to describe SI. There are three colors: red (r),
 294 blue(b) and green(g) and their corresponding three anti-colors; thus each quark carries
 295 one color unit while anti-quarks carries one anti-color unit. As said above, quarks are
 296 not allowed to be isolated due to the color confinement effect, therefore their features
 297 have been studied indirectly by observing their bound states created when:

- 298 • one quark with a color charge is attracted by an anti-quark with the correspond-
 299 ing anti-color charge forming a colorless particle called a “meson.”
- 300 • three quarks (anti-quarks) with different color (anti-color) charges are attracted
 301 among them forming a colorless particle called a “baryon(anti-baryon).”

302 In the first version of the quark model (1964), M. Gell-Mann [22] and G. Zweig [23,24]
 303 developed a consistent way to classify hadrons according to their properties. Only
 304 three quarks (u, d, s) were involved in a scheme in which all baryons have baryon
 305 number $B=1$ and therefore quarks have $B=1/3$; non-baryons have $B=0$. The scheme
 306 organize baryons in a two-dimensional space ($I_3 - Y$); Y (hypercharge) and I_3 (isospin)
 307 are quantum numbers related by the Gell-Mann-Nishijima formula [25, 26]:

$$Q = I_3 + \frac{Y}{2} \quad (2.2)$$

308 where $Y = B + S + C + T + B'$ are the quantum numbers listed in table 2.4. Baryon
 309 number is conserved in SI and EI which means that single quarks cannot be created
 310 but in pairs $q - \bar{q}$.

311

312 Similar to leptons, there are six quark flavors organized in three generations (see table
 313 2.1) and follow a mass hierarchy which again implies that higher generations decay

314 to first generation quarks.

	Quarks			T_3	Y_W	Leptons			T_3	Y_W
Doublets	$(\frac{u}{d'})_L$	$(\frac{c}{s'})_L$	$(\frac{t}{b'})_L$	$(\frac{1/2}{-1/2})$	$1/3$	$(\nu_e)_L$	$(\nu_\mu)_L$	$(\nu_\tau)_L$	$(\frac{1/2}{-1/2})$	-1
Singlets	u_R	c_R	t_R	0	$4/3$	ν_{eR}	$\nu_{\mu R}$	$\nu_{\tau R}$	0	-2
	d'_R	s'_R	b'_R	0	$-2/3$	e_R	μ_R	τ_R		

Table 2.5: Fermion weak isospin and weak hypercharge multiplets. Weak hypercharge is calculated through the Gell-Mann-Nishijima formula 2.2 but using the weak isospin and charge for quarks.

315

316 Isospin doublets of quarks are also defined (see table 2.5) and as for neutrinos, the
 317 mass eigenstates are not the same as the WI eigenstates which means that members of
 318 different quark generations are connected by the WI mediator; thus, up-type quarks
 319 are coupled not to down-type quarks directly but to a superposition of down-type
 320 quarks (q'_d) via WI according to:

$$q'_d = V_{CKM} q_d$$

321

$$\begin{pmatrix} d' \\ s' \\ b' \end{pmatrix} = \begin{pmatrix} V_{ud} & V_{us} & V_{ub} \\ V_{cd} & V_{cs} & V_{cb} \\ V_{td} & V_{ts} & V_{tb} \end{pmatrix} \begin{pmatrix} d \\ s \\ b \end{pmatrix} \quad (2.3)$$

322 where V_{CKM} is known as Cabibbo-Kobayashi-Maskawa (CKM) mixing matrix [27,28].
 323 The weak decays of quarks are represented in the diagram of figure 2.2; again the
 324 CKM matrix plays a central role since it contains the probabilities for the different
 325 quark decay channels, in particular, note that quark decays are greatly favored be-
 326 tween generation members.

327

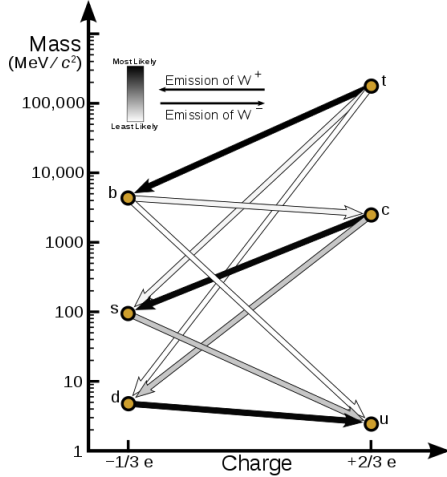


Figure 2.2: Transformations between quarks through WI. Higher generations quarks decay to first generation quarks by emitting a W boson. The arrow color indicates the likelihood of the transition according to the grey scale in the top left side which represent the CKM matrix parameters [29].

328 CKM matrix is a 3×3 unitary matrix parametrized by three mixing angles and the
 329 *CP-mixing phase*; the latter is the parameter responsible for the CP-violation in the
 330 SM. The fact that the b quark decays almost all the times to a top quark is exploited
 331 in this thesis when making the selection of the signal events by requiring the presence
 332 of a jet tagged as a jet comming from a b quark in the final state. The effect of the
 333 *CP-mixing phase* on the cross section of associated production of Higgs boson and a
 334 single top process is also explored in this thesis.

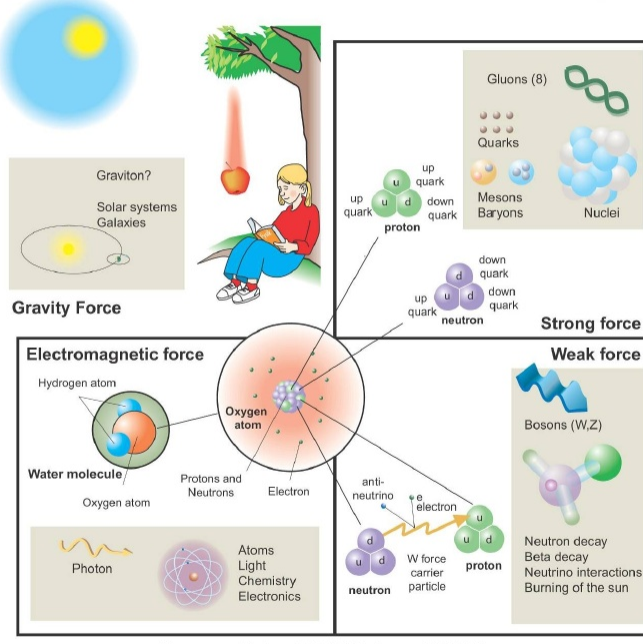
335 2.2.2 Fundamental interactions

336 Even though there are many manifestations of force in nature, like the ones repre-
 337 sented in figure 2.3, we can classify all of them into one of four fundamental interac-
 338 tions:

- 339 • *Electromagnetic interaction (EI)* affect particles that are “electrically charged,”
 340 like electrons and protons. It is described by QED combining quantum mechan-

Fundamental interactions.

Illustration: Typoform



Summer School KPI 15 August 2009

Figure 2.3: Fundamental interactions in nature. Despite the many manifestations of forces in nature, we can track all of them back to one of the fundamental interactions. The most common forces are gravity and electromagnetic given that all of us are subject and experience them in everyday life.

341 ics, special relativity and electromagnetism in order to explain how particles
 342 with electric charge interact through the exchange of photons, therefore, one
 343 says that “Electromagnetic Force” is mediated by “photons”. Figure 2.4a. shows
 344 a graphical representation, known as “feynman diagram”, of electron-electron
 345 scattering.

- 346 • *Strong interaction (SI)* described by Quantum Chromodynamics (QCD). Hadrons
 347 like proton and neutron have internal structure given that they are composed
 348 of two or more valence quarks⁵. Quarks have fractional electric charge which
 349 means that they are subject to electromagnetic interaction and in the case of the
 350 proton they should break apart due to electrostatic repulsion; however, quarks

⁵ particles made of four and five quarks are exotic states not so common

351 are held together inside the hadrons against their electrostatic repulsion by the
 352 “Strong Force” through the exchange of “gluons.” The analog to the electric
 353 charge is the “color charge”. Electrons and photons are elementary particles
 354 as quarks but they don’t carry color charge, therefore they are not subject to
 355 SI. The feynman diagram for gluon exchange between quarks is shown in figure
 356 2.4b.

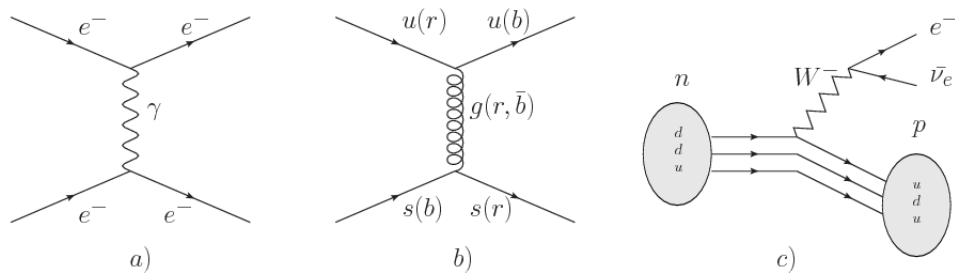


Figure 2.4: Feynman diagrams representing the interactions in SM; a) EI: e - e scattering;
 b) SI: gluon exchange between quarks ; c) WI: β -decay

357 • *Weak interaction (WI)* described by the Weak theory (WT), is responsible for
 358 instance for the radioactive decay in atoms and proton-proton (pp) fusion within
 359 the sun. Quarks and leptons are the particles affected by the weak interaction
 360 and posses a property called “flavor charge” which can be changed by emitting
 361 or absorbing one weak force mediator; they comes in six flavors each (see 2.2.1).
 362 There are three mediators of the “Weak force” known as “Z” boson in the case of
 363 electrically neutral changes and “ W^\pm ” bosons in the case of electrically charged
 364 changes. The “weak isospin” is the WI analog to electric charge in EI and color
 365 charge in SI and define how quarks and leptons are affected by the weak force.
 366 Figure 2.4c. shows the feynman diagram of β -decay where a newtron (n) is
 367 transformed in a proton (p) by emmiting a W^- particle. Since this thesis is in
 368 the frame of the electroweak interaction, a more detailed description of it will
 369 be given in section 2.3

- 370 • *Gravitational interaction (GI)* described by General Theory of Relativity (GR).
 371 It is responsible for the structure of galaxies and black holes as well as the
 372 expansion of the universe. As a classical theory, in the sense that it can be
 373 formulated without even appeal to the concept of quantization, it implies that
 374 the spacetime is a continuum and predictions can be made without limitation
 375 to the precision of the measurement tools which represent a direct contradiction
 376 of the quantum mechanics principles. Gravity is deterministic while quantum
 377 mechanics is probabilistic; despite that, efforts to develop a quantum theory of
 378 gravity have predicted the “graviton” as mediator of the Gravitational force⁶.

Interaction	Acts on	Relative strength	Range (m)	Mediators
Electromagnetic (QED)	Electrically charged particles	10^{-2}	Infinite	Photon
Strong (QCD)	Quarks and gluons	1	10^{-15}	Gluon
Weak (WI)	Leptons and quarks	10^{-6}	10^{-18}	W^\pm, Z
Gravitational (GI)	Massive particles	10^{-39}	Infinite	Graviton

Table 2.6: Fundamental interactions features [30].

- 379
- 380 Table 2.6 summarizes the main features of the fundamental interactions. The rela-
 381 tive strength of the fundamental forces reveals the meaning of strong and weak; in
 382 a context where the relative strength of the SI is 1, the EI is about hundred times
 383 weaker and WI is about million times weaker than the SI. A good description on
 384 how the relative strength and range of the fundamental interactions are calculated
 385 can be found in references [30,31]. In the everyday life, only EI and GI are explicitly
 386 experienced due to the range of these interactions; i.e., at the human scale distances
 387 only EI and GI have appreciable effects, in contrast to SI which at distances greater

⁶ Actually a wide variety of theories have been developed in an attempt to describe gravity; some famous examples are string theory and supergravity.

388 than 10^{-15} m become negligible.

389

390 QED was built successfully on the basis of the classical electrodynamics theory (CED)
 391 of Maxwell and Lorentz, following theoretical and experimental requirements imposed
 392 by

- 393 • lorentz invariance: independence on the reference frame.
- 394 • locality: interacting fields are evaluated at the same space-time point to avoid
 395 action at a distance.
- 396 • renormalizability: physical predictions are finite and well defined
- 397 • particle spectrum, symmetries and conservation laws already known must emerge
 398 from the theory.
- 399 • gauge invariance.

400 The gauge invariance requirement reflects the fact that the fundamental fields cannot
 401 be directly measured but associated fields which are the observables. Electric (“**E**”)
 402 and magnetic (“**B**”) fields in CED are associated with the electric scalar potential
 403 “**V**” and the vector potential “**A**”. In particular, **E** can be obtained by measuring
 404 the change in the space of the scalar potential (ΔV); however, two scalar potentials
 405 differing by a constant “ f ” correspond to the same electric field. The same happens in
 406 the case of the vector potential “**A**”; thus, different configurations of the associated
 407 fields result in the same set of values of the observables. The freedom in choosing
 408 one particular configuration is known as “gauge freedom”; the transformation law
 409 connecting two configurations is known as “gauge transformation” and the fact that
 410 the observables are not affected by a gauge transformation is called “gauge invariance”.

411 When the gauge transformation:

$$\begin{aligned} \mathbf{A} &\rightarrow \mathbf{A} - \Delta f \\ V &\rightarrow V - \frac{\partial f}{\partial t} \end{aligned} \tag{2.4}$$

412 is applied to Maxwell equations, they are still satisfied and the fields remain invariant.
 413 Thus, CED is invariant under gauge transformations and is called a “gauge theory”.
 414 The set of all gauge transformations form the “symmetry group” of the theory, which
 415 according to the group theory, has a set of “group generators”. The number of group
 416 generators determine the number of “gauge fields” of the theory.

417

418 As mentioned in the first lines of section 2.2, QED has one symmetry group ($U(1)$)
 419 with one group generator (the Q operator) and one gauge field (the electromagnetic
 420 field A^μ). In CED there is not a clear definition, beyond the historical convention, of
 421 which fields are the fundamental and which are the associated, but in QED it is clear
 422 that the fundamental field is A^μ . When a gauge theory is quantized, the gauge field
 423 is quantized and its quanta is called “gauge boson”. The word boson characterizes
 424 particles with integer spin which obvey Bose-einstein statistics.

425

426 As will be detailed in section 2.3, interactions between particles in a system can be
 427 obtained by considering first the Lagrangian density of free particles in the system,
 428 which of course is incomplete because the interaction terms have been left out, and
 429 demanding global phase transformation invariance. Global phase transformation in-
 430 variance means that a gauge transformation is performed identically to every point
 431 in the space⁷ and the Lagrangian remains invariant. Then, the global transformation

⁷ Here space corresponds to the 4-dimensional space i.e. space-time.

432 is promoted to a local phase transformation (this time the gauge transformation de-
 433 pends on the position in space) and again invariance is required.

434

435 Due to the space dependence of the local tranformation, the Lagrangian density is
 436 not invariant anymore. In order to restate the gauge invariance, the gauge covariant
 437 derivative is introduced in the Lagrangian and with it the gauge field responsible for
 438 the interaction between particles in the system. The new Lagrangian density is gauge
 439 invariant, includes the interaction terms needed to account for the interactions and
 440 provide a way to explain the interaction between particles through the exchange of
 441 the gauge boson.

442 This recipe was used to build QED and the theories that aim to explain the funda-
 443 mental interactions.

444 2.2.3 Gauge Bosons

445 The importance of the gauge bosons comes from the fact that they are the force
 446 mediators or force carriers. The features of the gauge bosons reflect the features of
 447 the fields they represent; these fetures are extracted from the Lagrangian density
 448 used to describe the interactions. In section 2.3, it will be shown how the gauge
 449 bosons of the EI and WI emerge from the electroweak Lagrangian. The SI gauge
 450 bosons features are also extracted from the SI Lagrangian but it is not detailed in
 451 this document. The main features of the SM gauge bosons will be briefly presented
 452 below and summarized in table 2.7.

453 • **Photon.** EI occurs when the photon couples to (is exchanged between) particles
 454 carrying electric charge; however, the photon itself does not carry electric charge,
 455 therefore, there is no coupling between photons. Given that the photon is

456 massless the EI is of infinite range, i.e., electrically charged particles interact
 457 even if they are located far away one from each other; this also implies that
 458 photons always move with the speed of light.

459 • **Gluon.** SI is mediated by gluons which, same as photons, are massless. They
 460 carry one unit of color charge and one unit of anticolor charge which means that
 461 gluons couple to other gluons. As a result, the range of the SI is not infinite
 462 but very short due to the attraction between gluons, giving rise to the “color
 463 confinement” which explains why color charged particles cannot be isolated but
 464 live within composited particles, like quarks inside protons.

465 • **W, Z.** The EWI mediators, W^\pm and Z, are massive which explains their short-
 466 range. Given that the WI is the only interaction that can change the flavor
 467 of the interacting particles, the W boson is the responsible for the nuclear
 468 transmutation where a neutron is converted in a proton or vice versa with the
 469 involvement of an electron and a neutrino (see figure 2.4c). The Z boson is the
 470 responsible of the neutral weak processes like neutrino elastic scattering where
 471 no electric charge but momentum transference is involved. WI gauge bosons
 472 carry isospin charge which makes possible the interaction between them.

Interaction	Mediator	Electric charge (e)	Color charge	Weak Isospin	mass (GeV/c ²)
Electromagnetic	Photon (γ)	0	No	0	0
Strong	Gluon (g)	0	Yes -octet	No	0
Weak	W^\pm Z	± 1 0	No	± 1 0	80.385 ± 0.015 91.188 ± 0.002

Table 2.7: SM gauge bosons main features [21].

474 2.3 Electroweak unification and the Higgs

475 mechanism

476 Physicists dreams of building a theory that contains all the interactions in one single
 477 interaction, i.e., showing that at some scale in energy all the four fundamental in-
 478 teractions are unified and only one interaction emerges in a “Theory of everything”.
 479 The first sign of the feasibility of such unification comes from success in the con-
 480 struction of the CED. Einstein spent years trying to reach that dream, which by
 481 1920 only involved electromagnetism and gravity, with no success; however, a new
 482 partial unification was achieved in the 1960’s, when S.Glashow [14], A.Salam [15] and
 483 S.Weinberg [16] independently proposed that electromagnetic and weak interactions
 484 are two manifestations of a more general interaction called “electroweak interaction
 485 (EWT).” QCD and EWT were developed in parallel and following the useful prescrip-
 486 tion provided by QED and the gauge invariance principles.

487

488 The theory of weak interactions was capable of explaining the β -decay and in general
 489 the processes mediated by W^\pm bosons. However, there were some processes like the
 490 “ $\nu_\mu - e$ scattering” which would require the exchange of two W bosons (see figure 2.5
 491 top diagrams) giving rise to divergent loop integrals and then non finite predictions.
 492 By including neutral currents involving fermions via the exchange of neutral bosons
 493 Z, those divergences are compensated and the predictions become realistic.
 494 Neutral weak interaction vertices conserve flavor in the same way as the electromag-
 495 netic vertices do, but additionally, the Z boson can couple to neutrinos which implies
 496 that processes involving charged fermions can proceed through EI or WI but processes
 497 involving neutrinos can proceed only through WI.

498

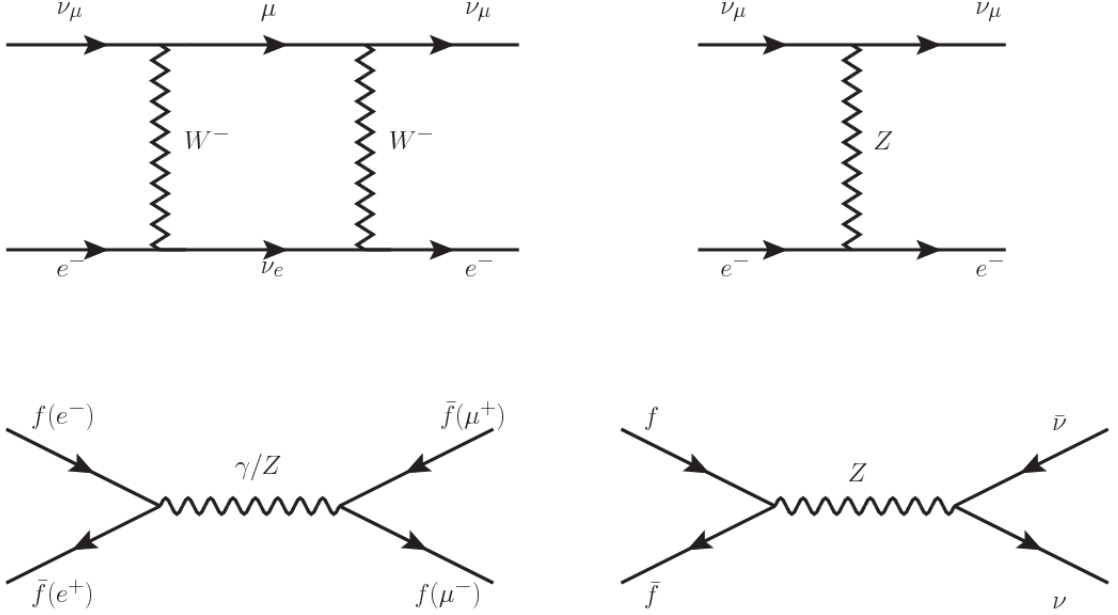


Figure 2.5: Top: $\nu_\mu - e^-$ scattering going through charged currents (left) and neutral currents (right). Bottom: neutral current processes for charged fermions (left) and involving neutrinos (right). While neutral current processes involving only charged fermions can proceed through EI or WI, those involving neutrinos can only proceed via WI.

499 The prescription to build a gauge theory of the WI consist of proposing a free field La-
500 grangian density that includes the particles involved; next, by requesting invariance
501 under global phase transformations first and generalizing to local phase transfor-
502 mations invariance later, the conserved currents are identified and interactions are
503 generated by introducing gauge fields. Given that the goal is to include the EI and
504 WI in a single theory, the group symmetry considered should be a combination of
505 $SU(2)_L$ and $U(1)_{em}$, however the latter cannot be used directly because the EI treat
506 left and right-handed particles indistinctly in contrast to the former. Fortunately, the
507 weak hypercharge, which is a combination of the weak isospin and the electric charge
508 (eqn 2.2) is suitable to be used since it is conserved by the EI and WI. Thus, the
509 symmetry group to be considered is

$$G \equiv SU(2)_L \otimes U(1)_Y \quad (2.5)$$

510 The following treatment applies to any of the fermion generations, but for simplicity
 511 the first generation of leptons will be considered [2, 3, 32, 33].

512

513 Given the first generation of leptons

$$\psi_1 = \begin{pmatrix} \nu_e \\ e^- \end{pmatrix}_L, \quad \psi_2 = \nu_{eR}, \quad \psi_3 = e_R^- \quad (2.6)$$

514 the charged fermionic currents are given by

$$J_\mu \equiv J_\mu^+ = \bar{\nu}_{eL} \gamma_\mu e_L, \quad J_\mu^\dagger \equiv J_\mu^- = \bar{e}_L \gamma_\mu \nu_{eL} \quad (2.7)$$

515 and the free Lagrangian is given by

$$\mathcal{L}_0 = \sum_{j=1}^3 i\bar{\psi}_j(x) \gamma^\mu \partial_\mu \psi_j(x). \quad (2.8)$$

516 Mass terms are included directly in the QED and QCD free Lagrangians since they
 517 preserve the invariance under the symmetry transformations involved which treat
 518 left-handed and right-handed similarly, however mass terms of the form

$$m_W^2 W_\mu^\dagger(x) W^\mu(x) + \frac{1}{2} m_Z^2 Z_\mu(x) Z^\mu(x) - m_e \bar{\psi}_e(x) \psi_e(x) \quad (2.9)$$

519 which represent the mass of W^\pm , Z and electrons, are not invariant under G trans-
 520 formations, therefore the gauge fields described by the EWI are in principle massless.

521

522 Experiments have shown that the gauge fields are not massless; however, they have

523 to acquire mass through a mechanism compatible with the gauge invariance; that
 524 mechanism is known as the “Higgs mechanism” and will be considered later in this
 525 section. The global transformations in the combined symmetry group G can be
 526 written as

$$\begin{aligned}\psi_1(x) &\xrightarrow{G} \psi'_1(x) \equiv U_Y U_L \psi_1(x), \\ \psi_2(x) &\xrightarrow{G} \psi'_2(x) \equiv U_Y \psi_2(x), \\ \psi_3(x) &\xrightarrow{G} \psi'_3(x) \equiv U_Y \psi_3(x)\end{aligned}\tag{2.10}$$

527 where U_L represent the $SU(2)_L$ transformation acting only on the weak isospin dou-
 528 blet and U_Y represent the $U(1)_Y$ transformation acting on all the weak isospin mul-
 529 tiplets. Explicitly

$$U_L \equiv \exp\left(i \frac{\sigma_i}{2} \alpha^i\right), \quad U_Y \equiv \exp(i y_i \beta) \quad (i = 1, 2, 3)\tag{2.11}$$

530 with σ_i the Pauli matrices and y_i the weak hypercharges. In order to promote the
 531 transformations from global to local while keeping the invariance, it is required that
 532 $\alpha^i = \alpha^i(x)$, $\beta = \beta(x)$ and the replacement of the ordinary derivatives by the covariant
 533 derivatives

$$\begin{aligned}D_\mu \psi_1(x) &\equiv [\partial_\mu + ig\sigma_i W_\mu^i(x)/2 + ig'y_1 B_\mu(x)] \psi_1(x) \\ D_\mu \psi_2(x) &\equiv [\partial_\mu + ig'y_2 B_\mu(x)] \psi_2(x) \\ D_\mu \psi_3(x) &\equiv [\partial_\mu + ig'y_3 B_\mu(x)] \psi_3(x)\end{aligned}\tag{2.12}$$

534 introducing in this way four gauge fields, $W_\mu^i(x)$ and $B_\mu(x)$, in the process. The
 535 covariant derivatives (eqn 2.12) are required to transform in the same way as fermion
 536 fields $\psi_i(x)$ themselves, therefore, the gauge fields transform as:

$$\begin{aligned} B_\mu(x) &\xrightarrow{G} B'_\mu(x) \equiv B_\mu(x) - \frac{1}{g'} \partial_\mu \beta(x) \\ W_\mu^i(x) &\xrightarrow{G} W_\mu^{i\prime}(x) \equiv W_\mu^i(x) - \frac{i}{g} \partial_\mu \alpha_i(x) - \varepsilon_{ijk} \alpha_i(x) W_\mu^j(x). \end{aligned} \quad (2.13)$$

537 The G invariant version of the Lagrangian density 2.8 can be written as

$$\mathcal{L}_0 = \sum_{j=1}^3 i \bar{\psi}_j(x) \gamma^\mu D_\mu \psi_j(x) \quad (2.14)$$

538 where free massless fermion and gauge fields and fermion-gauge boson interactions
 539 are included. The EWI Lagrangian density must additionally include kinetic terms
 540 for the gauge fields (\mathcal{L}_G) which are built from the field strengths, according to

$$B_{\mu\nu}(x) \equiv \partial_\mu B_\nu - \partial_\nu B_\mu \quad (2.15)$$

$$W_{\mu\nu}^i(x) \equiv \partial_\mu W_\nu^i(x) - \partial_\nu W_\mu^i(x) - g \varepsilon^{ijk} W_\mu^j W_\nu^k \quad (2.16)$$

541 the last term in eqn. 2.16 is added in order to hold the gauge invariance; therefore,

$$\mathcal{L}_G = -\frac{1}{4} B_{\mu\nu}(x) B^{\mu\nu}(x) - \frac{1}{4} W_{\mu\nu}^i(x) W_i^{\mu\nu}(x) \quad (2.17)$$

542 which contains not only the free gauge fields contributions, but also the gauge fields
 543 self-interactions and interactions among them.

544 The three weak isospin conserved currents resulting from the $SU(2)_L$ symmetry are

545 given by

$$J_\mu^i(x) = \frac{1}{2} \bar{\psi}_1(x) \gamma_\mu \sigma^i \psi_1(x) \quad (2.18)$$

546 while the weak hypercharge conserved current resulting from the $U(1)_Y$ symmetry is
 547 given by

$$J_\mu^Y = \sum_{j=1}^3 \bar{\psi}_j(x) \gamma_\mu y_j \psi_j(x) \quad (2.19)$$

548 In order to evaluate the electroweak interactions modeled by an isovector field W_μ^i
 549 which couples to isospin currents J_μ^i with strength g and additionally the singlet
 550 field B_μ which couples to the weak hypercharge current J_μ^Y with strength $g'/2$. The
 551 interaction Lagrangian density to be considered is

$$\mathcal{L}_I = -g J^{i\mu}(x) W_\mu^i(x) - \frac{g'}{2} J^{Y\mu}(x) B_\mu(x) \quad (2.20)$$

552 Note that the weak isospin currents are not the same as the charged fermionic currents
 553 that were used to describe the WI (eqn 2.7), since the weak isospin eigenstates are
 554 not the same as the mass eigenstates, but they are closely related

$$J_\mu = \frac{1}{2} (J_\mu^1 + i J_\mu^2), \quad J_\mu^\dagger = \frac{1}{2} (J_\mu^1 - i J_\mu^2). \quad (2.21)$$

555 The same happens with the gauge fields W_μ^i which are related to the mass eigenstates
 556 W^\pm by

$$W_\mu^+ = \frac{1}{\sqrt{2}} (W_\mu^1 - i W_\mu^2), \quad W_\mu^- = \frac{1}{\sqrt{2}} (W_\mu^1 + i W_\mu^2). \quad (2.22)$$

557 The fact that there are three weak isospin conserved currents is an indication that in

558 addition to the charged fermionic currents, which couple charged to neutral leptons,
 559 there should be a neutral fermionic current that couples neutral fermions or electri-
 560 cally charged fermions that have the same electric charge and thus electric charge
 561 change is not implied. The third weak isospin current contains a term that is simi-
 562 lar to the electromagnetic current (j_μ^{em}), indicating that there is a relation between
 563 them and resembling the Gell-Mann-Nishijima formula 2.2 adapted to electroweak
 564 interactions

$$Q = T_3 + \frac{Y_W}{2}. \quad (2.23)$$

565 Just as Q generates the $U(1)_{em}$ symmetry, the weak hypercharge generates the $U(1)_Y$
 566 symmetry as said before. It is possible to write the relationship in terms of the currents
 567 as

$$j_\mu^{em} = J_\mu^3 + \frac{1}{2}J_\mu^Y. \quad (2.24)$$

568 The neutral gauge fields W_μ^3 and B_μ cannot be directly identified with the Z and the
 569 photon fields since the photon interacts similarly with left and right-handed fermions;
 570 however, they are related through a linear combination given by

$$A_\mu = B_\mu \cos \theta_W + W_\mu^3 \sin \theta_W \quad (2.25)$$

$$Z_\mu = -B_\mu \sin \theta_W + W_\mu^3 \cos \theta_W$$

571 where θ_W is known as the “Weinberg angle.” The interaction Lagrangian is now given
 572 by

$$\mathcal{L}_I = -\frac{g}{\sqrt{2}}(J^\mu W_\mu^+ + J^{\mu\dagger} W_\mu^-) - \left(g \sin \theta_W J_\mu^3 + g' \cos \theta_W \frac{J_\mu^Y}{2}\right) A^\mu - \left(g \cos \theta_W J_\mu^3 - g' \sin \theta_W \frac{J_\mu^Y}{2}\right) Z^\mu \quad (2.26)$$

573 the first term is the weak charged current interaction, while the second term is the
 574 electromagnetic interaction under the condition

$$g \sin \theta_W = g' \cos \theta_W = e, \quad \frac{g'}{g} = \tan \theta_W \quad (2.27)$$

575 contained in the eqn.2.24; the third term is the neutral weak current.

576 Note that the neutral fields transformation given by the eqn. 2.25 can be written in
 577 terms of the coupling constants g and g' as:

$$A_\mu = \frac{g' W_\mu^3 + g B_\mu}{\sqrt{g^2 + g'^2}}, \quad Z_\mu = \frac{g W_\mu^3 - g' B_\mu}{\sqrt{g^2 + g'^2}} \quad (2.28)$$

578 So far, the Lagrangian density describing the non-massive EWI is:

$$\mathcal{L}_{nmEWI} = \mathcal{L}_0 + \mathcal{L}_G \quad (2.29)$$

579 where fermion and gauge fields have been considered massless because their regular
 580 mass terms are manifestly non invariant under G transformations; therefore, masses
 581 have to be generated in a gauge invariant way. The mechanism by which this goal is
 582 achieved is known as the “Higgs mechanism” and is closely connected to the concept
 583 of “spontaneous symmetry breaking.”

584 2.3.1 Spontaneous symmetry breaking

585 Figure 2.6 left shows a steel nail (top) which is subject to an external force; the form
 586 of the potential energy is also shown (bottom).

587 Before reaching the critical force value, the system has rotational symmetry with re-
 588 spect to the nail axis; however, after the critical force value is reached the nail buckles

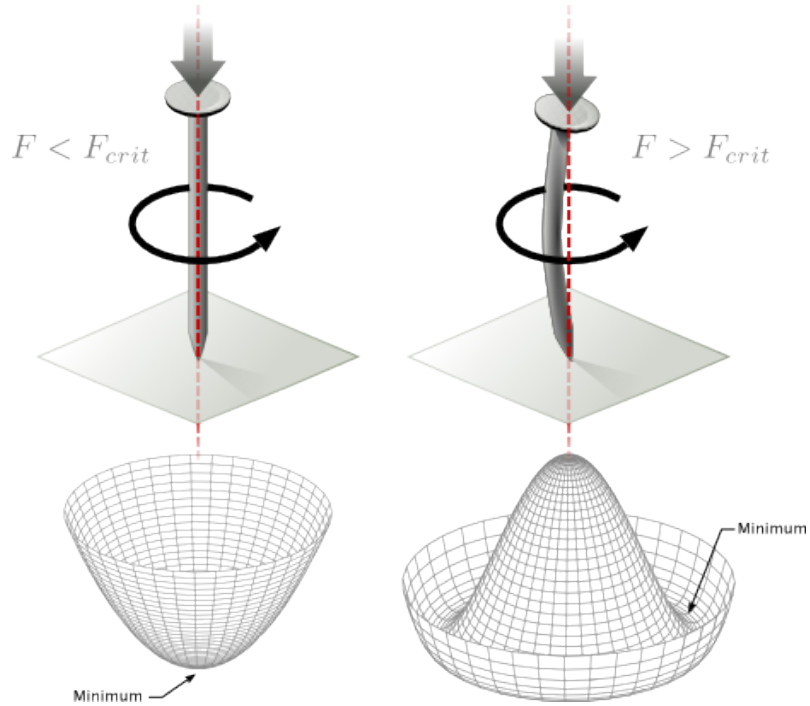


Figure 2.6: Spontaneous symmetry breaking mechanism. The steel nail, subject to an external force (top left), has rotational symmetry with respect to its axis. When the external force overcomes a critical value the nail buckles (top right) choosing a minimal energy state (ground state) and thus “*breaking spontaneously the rotational symmetry*”. The potential energy (bottom) changes but holds the rotational symmetry; however, an infinite number of asymmetric ground states are generated and circularly distributed in the bottom of the potential [34].

589 (top right). The form of the potential energy (bottom right) changes, preserving its
 590 rotational symmetry although its minima does not exhibit that rotational symmetry
 591 any longer. Right before the nail buckles there is no indication of the direction the
 592 nail will bend because any of the directions are equivalent, but once the nail bent,
 593 choosing a direction, an arbitrary minimal energy state (ground state) is selected and
 594 it does not share the system rotational symmetry. This mechanism for reaching an
 595 asymmetric ground state is known as “*spontaneous symmetry breaking (SSB)*”.
 596 The lesson from this analysis is that the way to introduce the SSB mechanism into a
 597 system is by adding the appropriate potential to it.

599 Figure 2.7 shows a plot of the potential $V(\phi)$ in the case of a scalar field ϕ

$$V(\phi) = \mu^2 \phi^\dagger \phi + \lambda (\phi^\dagger \phi)^2 \quad (2.30)$$

600 If $\mu^2 > 0$ the potential has only one minimum at $\phi = 0$ and describes a scalar field
 601 with mass μ . If $\mu^2 < 0$ the potential has a local maximum at $\phi = 0$ and two minima
 602 at $\phi = \pm\sqrt{-\mu^2/\lambda}$ which enables the SSB mechanism to work.

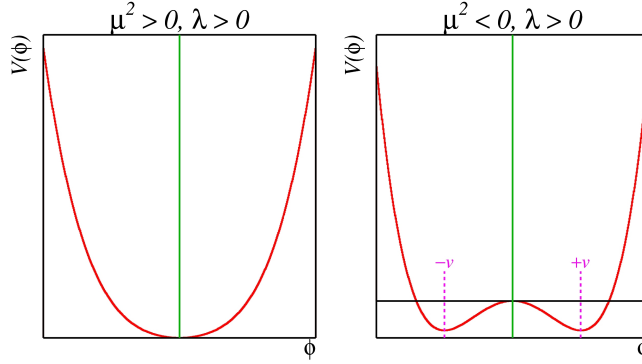


Figure 2.7: Shape of the potential $V(\phi)$ for $\lambda > 0$ and: $\mu^2 > 0$ (left) and $\mu^2 < 0$ (right). The case $\mu^2 < 0$ corresponds to the potential suitable for introducing the SSB mechanism by choosing one of the two ground states which are connected via reflection symmetry. [34].

603 In the case of a complex scalar field $\phi(x)$

$$\phi(x) = \frac{1}{\sqrt{2}}(\phi_1 + i\phi_2) \quad (2.31)$$

604 the Lagrangian (invariant under global $U(1)$ transformations) is given by

$$\mathcal{L} = (\partial_\mu \phi)^\dagger (\partial^\mu \phi) - V(\phi), \quad V(\phi) = \mu^2 \phi^\dagger \phi + \lambda (\phi^\dagger \phi)^2 \quad (2.32)$$

605 where an appropriate potential has been added in order to introduce the SSB.

606 As seen in figure 2.8, the potential has now an infinite number of minima circularly
 607 distributed along the ξ -direction which makes possible the occurrence of the SSB by

608 choosing an arbitrary ground state; for instance, $\xi = 0$, i.e. $\phi_1 = v, \phi_2 = 0$

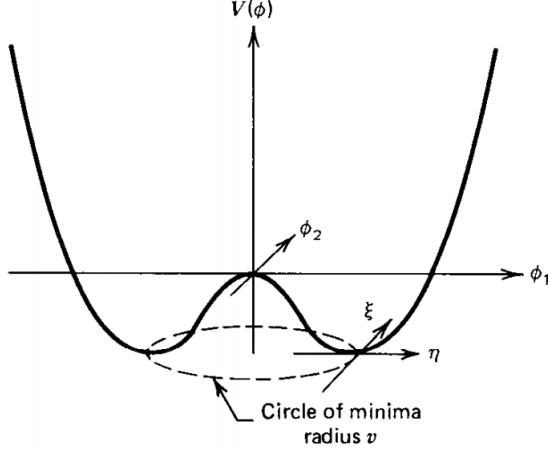


Figure 2.8: Potential for complex scalar field. There is a circle of minima of radius v along the ξ -direction [3].

$$\phi_0 = \frac{v}{\sqrt{2}} \exp(i\xi) \quad \xrightarrow{\text{SSB}} \quad \phi_0 = \frac{v}{\sqrt{2}} \quad (2.33)$$

609 As usual, excitations over the ground state are studied by making an expansion about
610 it; thus, the excitation can be parametrized as:

$$\phi(x) = \frac{1}{\sqrt{2}}(v + \eta(x) + i\xi(x)) \quad (2.34)$$

611 which when substituted into eqn. 2.32 produces a Lagrangian in terms of the new
612 fields η and ξ

$$\mathcal{L}' = \frac{1}{2}(\partial_\mu \xi)^2 + \frac{1}{2}(\partial_\mu \eta)^2 + \mu^2 \eta^2 - V(\phi_0) - \lambda v \eta (\eta^2 + \xi^2) - \frac{\lambda}{4}(\eta^2 + \xi^2)^2 \quad (2.35)$$

613 where the last two terms represent the interactions and self-interaction between the
614 two fields η and ξ . The particular feature of the SSB mechanism is revealed when

615 looking to the first three terms of \mathcal{L}' . Before the SSB, only the massless ϕ field is
 616 present in the system; after the SSB there are two fields of which the η -field has
 617 acquired mass $m_\eta = \sqrt{-2\mu^2}$ while the ξ -field is still massless (see figure 2.9).

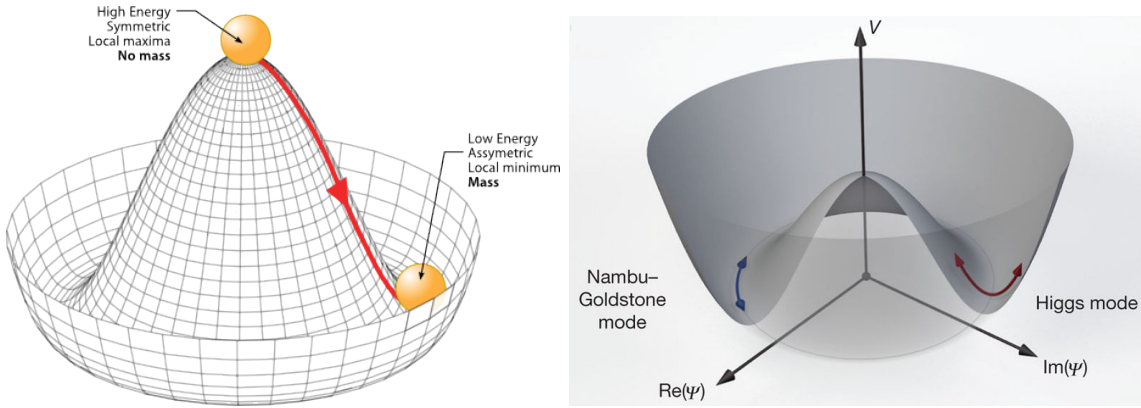


Figure 2.9: SSB mechanism for a complex scalar field [34, 35].

618 Thus, *the SSB mechanism serves as a method to generate mass but as a side effect a*
 619 *massless field is introduced in the system.* This fact is known as the Goldstone theorem
 620 and states that a massless scalar field appears in the system for each continuous
 621 symmetry spontaneously broken. Another version of the Goldstone theorem states
 622 that “*if a Lagrangian is invariant under a continuous symmetry group G , but the*
 623 *vacuum is only invariant under a subgroup $H \subset G$, then there must exist as many*
 624 *massless spin-0 particles (Nambu-Goldstone bosons) as broken generators.*” [33] The
 625 Nambu-Goldstone boson can be understood considering that the potential in the ξ -
 626 direction is flat so excitations in that direction are not energy consuming and thus
 627 represent a massless state.

628 2.3.2 Higgs mechanism

629 When the SSB mechanism is introduced in the formulation of the EWI in an attempt
 630 to generate the mass of the so far massless gauge bosons and fermions, an interesting

631 effect is revealed. In order to keep the G symmetry group invariance and generate
 632 the mass of the EW gauge bosons, a G invariant Lagrangian density (\mathcal{L}_S) has to be
 633 added to the non massive EWI Lagrangian (eqn. 2.29)

$$\mathcal{L}_S = (D_\mu \phi)^\dagger (D^\mu \phi) - \mu^2 \phi^\dagger \phi - \lambda (\phi^\dagger \phi)^2, \quad \lambda > 0, \mu^2 < 0 \quad (2.36)$$

$$D_\mu \phi = \left(i\partial_\mu - g \frac{\sigma_i}{2} W_\mu^i - g' \frac{Y}{2} B_\mu \right) \phi \quad (2.37)$$

634 ϕ has to be an isospin doublet of complex scalar fields so it preserves the G invariance;
 635 thus ϕ can be defined as:

$$\phi = \begin{pmatrix} \phi^+ \\ \phi^0 \end{pmatrix} \equiv \frac{1}{\sqrt{2}} \begin{pmatrix} \phi_1 + i\phi_2 \\ \phi_3 + i\phi_4 \end{pmatrix}. \quad (2.38)$$

636 The minima of the potential are defined by

$$\phi^\dagger \phi = \frac{1}{2} (\phi_1^2 + \phi_2^2 + \phi_3^2 + \phi_4^2) = -\frac{\mu^2}{2\lambda}. \quad (2.39)$$

637 The choice of the ground state is critical. By choosing a ground state, invariant under
 638 $U(1)_{em}$ gauge symmetry, the photon will remain massless and the W^\pm and Z bosons
 639 masses will be generated which is exactly what is needed. In that sense, the best
 640 choice corresponds to a weak isospin doublet with $T_3 = -1/2$, $Y_W = 1$ and $Q = 0$
 641 which defines a ground state with $\phi_1 = \phi_2 = \phi_4$ and $\phi_3 = v$:

$$\phi_0 \equiv \frac{1}{\sqrt{2}} \begin{pmatrix} 0 \\ v \end{pmatrix}, \quad v^2 \equiv -\frac{\mu^2}{\lambda}. \quad (2.40)$$

642 where the vacuum expectation value v is fixed by the Fermi coupling G_F according
 643 to $v = (\sqrt{2}G_F)^{1/2} \approx 246$ GeV.

644 The G symmetry has been broken and three Nambu-Goldstone bosons will appear.

645 The next step is to expand ϕ about the chosen ground state as:

$$\phi(x) = \frac{1}{\sqrt{2}} \exp\left(\frac{i}{v} \sigma_i \theta^i(x)\right) \begin{pmatrix} 0 \\ v + H(x) \end{pmatrix} \approx \frac{1}{\sqrt{2}} \begin{pmatrix} \theta_1(x) + i\theta_2(x) \\ v + H(x) - i\theta_3(x) \end{pmatrix} \quad (2.41)$$

646 to describe fluctuations from the ground state ϕ_0 . The fields $\theta_i(x)$ represent the
 647 Nambu-Goldstone bosons while $H(x)$ is known as “higgs field.” The fundamental
 648 feature of the parametrization used is that the dependence on the $\theta_i(x)$ fields is
 649 factored out in a global phase that can be eliminated by taking the physical “unitary
 650 gauge” $\theta_i(x) = 0$. Therefore the expansion about the ground state is given by:

$$\phi(x) \frac{1}{\sqrt{2}} \begin{pmatrix} 0 \\ v + H(x) \end{pmatrix} \quad (2.42)$$

651 which when substituted into \mathcal{L}_S (eqn. 2.36) results in a Lagrangian containing the now
 652 massive three gauge bosons W^\pm, Z , one massless gauge boson (photon) and the new
 653 Higgs field (H). The three degrees of freedom corresponding to the Nambu-Goldstone
 654 bosons are now integrated into the massive gauge bosons as their longitudinal polar-
 655 izations which were not available when they were massless particles. The effect by
 656 which vector boson fields acquire mass after an spontaneous symmetry breaking but
 657 without an explicit gauge invariance breaking is known as the “*Higgs mechanism*.”
 658 The mechanism was proposed by three independent groups: F.Englert and R.Brout
 659 in August 1964 [36], P.Higgs in October 1964 [37] and G.Guralnik, C.Hagen and
 660 T.Kibble in November 1964 [38]; however, its importance was not realized until
 661 S.Glashow [14], A.Salam [15] and S.Weinberg [16], independently, proposed that elec-
 662 tromagnetic and weak interactions are two manifestations of a more general interac-
 663 tion called “electroweak interaction” in 1967.

664 **2.3.3 Masses of the gauge bosons**

665 The mass of the gauge bosons is extracted by evaluating the kinetic part of Lagrangian

666 \mathcal{L}_S in the ground state (known also as the vacuum expectation value), i.e.,

$$\left| \left(\partial_\mu - ig \frac{\sigma_i}{2} W_\mu^i - i \frac{g'}{2} B_\mu \right) \phi_0 \right|^2 = \left(\frac{1}{2} v g \right)^2 W_\mu^+ W^{-\mu} + \frac{1}{8} v^2 (W_\mu^3, B_\mu) \begin{pmatrix} g^2 & -gg' \\ -gg' & g'^2 \end{pmatrix} \begin{pmatrix} W^{3\mu} \\ B^\mu \end{pmatrix} \quad (2.43)$$

667 comparing with the typical mass term for a charged boson $M_W^2 W^+ W^-$

$$M_W = \frac{1}{2} v g. \quad (2.44)$$

The second term in the right side of the eqn.2.43 comprises the masses of the neutral bosons, but it needs to be written in terms of the gauge fields Z_μ and A_μ in order to be compared to the typical mass terms for neutral bosons, therefore using eqn. 2.28

$$\begin{aligned} \frac{1}{8} v^2 [g^2 (W_\mu^3)^2 - 2gg' W_\mu^3 B^\mu + g'^2 B_\mu^2] &= \frac{1}{8} v^2 [g W_\mu^3 - g' B_\mu]^2 + 0[g' W_\mu^3 + g B_\mu]^2 \quad (2.45) \\ &= \frac{1}{8} v^2 [\sqrt{g^2 + g'^2} Z_\mu]^2 + 0[\sqrt{g^2 + g'^2} A_\mu]^2 \end{aligned}$$

668 and then

$$M_Z = \frac{1}{2} v \sqrt{g^2 + g'^2}, \quad M_A = 0 \quad (2.46)$$

669 **2.3.4 Masses of the fermions**

670 The lepton mass terms can be generated by introducing a gauge invariant Lagrangian
 671 term describing the Yukawa coupling between the lepton field and the Higgs field

$$\mathcal{L}_{Yl} = -G_l \left[(\bar{\nu}_l, \bar{l})_L \begin{pmatrix} \phi^+ \\ \phi^0 \end{pmatrix} l_R + \bar{l}_R (\phi^-, \bar{\phi}^0) \begin{pmatrix} \nu_l \\ l \end{pmatrix}_L \right], \quad l = e, \mu, \tau. \quad (2.47)$$

672 After the SSB and replacing the usual field expansion about the ground state (eqn.2.40)
 673 into \mathcal{L}_{Yl} , the mass term arises

$$\mathcal{L}_{Yl} = -m_l (\bar{l}_L l_R + \bar{l}_R l_L) - \frac{m_l}{v} (\bar{l}_L l_R + \bar{l}_R l_L) H = -m_l \bar{l} l \left(1 + \frac{H}{v} \right) \quad (2.48)$$

674

$$m_l = \frac{G_l}{\sqrt{2}} v \quad (2.49)$$

675 where the additional term represents the lepton-Higgs interaction. The quark masses
 676 are generated in a similar way as lepton masses but for the upper member of the
 677 quark doublet a different Higgs doublet is needed:

$$\phi_c = -i\sigma_2 \phi^* = \begin{pmatrix} -\bar{\phi}^0 \\ \phi^- \end{pmatrix}. \quad (2.50)$$

678 Additionally, given that the quark isospin doublets are not constructed in terms of
 679 the mass eigenstates but in terms of the flavor eigenstates, as shown in table2.5, the
 680 coupling parameters will be related to the CKM matrix elements; thus the quark
 681 Lagrangian is given by:

$$\mathcal{L}_{Yq} = -G_d^{i,j} (\bar{u}_i, \bar{d}'_i)_L \begin{pmatrix} \phi^+ \\ \phi^0 \end{pmatrix} d_{jR} - G_u^{i,j} (\bar{u}_i, \bar{d}'_i)_L \begin{pmatrix} -\bar{\phi}^0 \\ \phi^- \end{pmatrix} u_{jR} + h.c. \quad (2.51)$$

682 with $i,j=1,2,3$. After SSB and expansion about the ground state, the diagonal form

683 of \mathcal{L}_{Yq} is:

$$\mathcal{L}_{Yq} = -m_d^i \bar{d}_i d_i \left(1 + \frac{H}{v}\right) - m_u^i \bar{u}_i u_i \left(1 + \frac{H}{v}\right) \quad (2.52)$$

684 Fermion masses depend on arbitrary couplings G_l and $G_{u,d}$ and are not predicted by
685 the theory.

686 2.3.5 The Higgs field

687 After the characterization of the fermions and gauge bosons as well as their interac-
688 tions, it is necessary to characterize the Higgs field itself. The Lagrangian \mathcal{L}_S in eqn.
689 2.36 written in terms of the gauge bosons is given by

$$\mathcal{L}_S = \frac{1}{4} \lambda v^4 + \mathcal{L}_H + \mathcal{L}_{HV} \quad (2.53)$$

690

$$\mathcal{L}_H = \frac{1}{2} \partial_\mu H \partial^\mu H - \frac{1}{2} m_H^2 H^2 - \frac{1}{2v} m_H^2 H^3 - \frac{1}{8v^2} m_H^2 H^4 \quad (2.54)$$

691

$$\mathcal{L}_{HV} = m_H^2 W_\mu^+ W^{\mu-} \left(1 + \frac{2}{v} H + \frac{2}{v^2} H^2\right) + \frac{1}{2} m_Z^2 Z_\mu Z^\mu \left(1 + \frac{2}{v} H + \frac{2}{v^2} H^2\right) \quad (2.55)$$

692 The mass of the Higgs boson is deduced as usual from the mass term in the Lagrangian
693 resulting in:

$$m_H = \sqrt{-2\mu^2} = \sqrt{2\lambda}v \quad (2.56)$$

694 however, it too is not predicted by the theory. The experimental efforts to find the
695 Higgs boson, carried out by the CMS and ATLAS experiments⁸, gave great results
696 by July of 2012 when the discovery of a new particles was announced and which
697 is compatible with the Higgs boson predicted by the electroweak theory [39, 40].
698 Although at the announcement time there were some reservations about calling the

⁸ CMS stands for Compact Muon Solenoid; ATLAS stand for A Toroidal LHC Apparatus. Both are general experiments held at the Large Hadron Collider(LHC)

699 new particle the “Higgs boson”, today this name is widely accepted. The result of
 700 the measurement of the Higgs mass reported by both experiments [41] is in table 2.8.

Property	Value
Electric charge	0
Colour charge	0
Spin	0
Weak isospin	$-1/2$
Weak hypercharge	1
Parity	1
Mass (GeV/c^2)	$125.09 \pm 0.21 \text{ (stat.)} \pm 0.11 \text{ (syst.)}$

Table 2.8: Higgs boson properties. Higgs mass is not predicted by the theory and the value here corresponds to the experimental measurement.

701

702 **2.3.6 Higgs boson production mechanisms at LHC.**

703 At LHC, Higgs boson is produced as a result of the collision of two counter-rotating
 704 protons beams. A detailed description of the LHC machine will be presented in the
 705 chapter 3. “The total cross section” is the parameter that quantify the number of pp
 706 collisions that happen when a number of protons are fired at each other. Different
 707 results can be obtained after a pp collision and for each one the “cross section” is
 708 defined as the number of pp collisions that conclude in that particular result with
 709 respect to the number of protons fired at each other.

710 Protons are composed of quarks and these quarks are bound by gluons; however, what
 711 is commonly called the quark content of the proton makes reference to the valence
 712 quarks. A sea of quarks and gluons is also present inside the proton as represented
 713 in figure 2.10. In a proton-proton (pp) collision, the constituents (quarks and gluons)
 714 are those who collide. The pp cross section depends on the momentum of the colliding
 715 particles, reason for which it is needed to know how the momentum is distributed
 716 inside the proton. Quarks and gluons are known as partons and the functions that

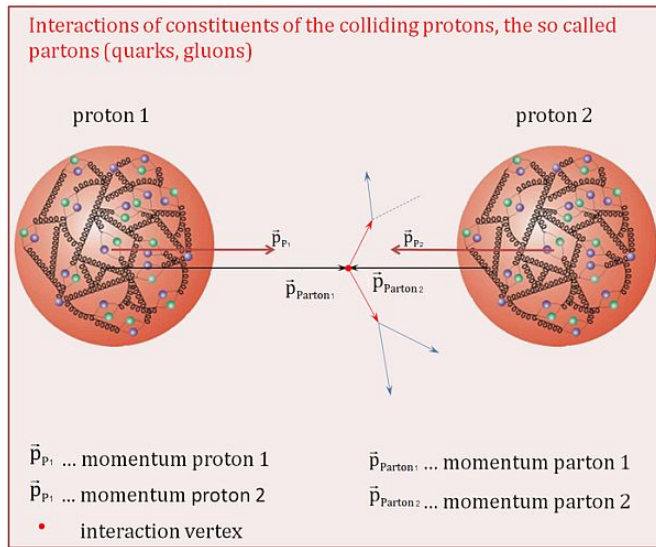


Figure 2.10: Proton-proton collision. Protons are composed of 3 valence quarks, a sea of quarks and gluons; therefore in a proton-proton collision, quarks and gluons are those who collide. [45].

describes how the proton momentum is distributed among partons inside it are called
“parton distribution functions (PDFs)”; PDFs are determined from experimental data
obtained in experiments where the internal structure of hadrons is tested.

In addition, in physics, a common approach to study complex systems consists in starting with a simpler version of them, for which a well known description is available, and add an additional “perturbation” which represent a small deviation from the known behavior. If the perturbation is small enough, the physical quantities associated with the perturbed system are expressed as a series of corrections to those of the simpler system; therefore, the more terms are considered in the series (the higher order in the perturbation series), the more precise is the the description of the complex system.

This thesis explores the Higgs production at LHC; therefore the overview presented here will be oriented specifically to the production mechanisms after pp collisions at LHC.

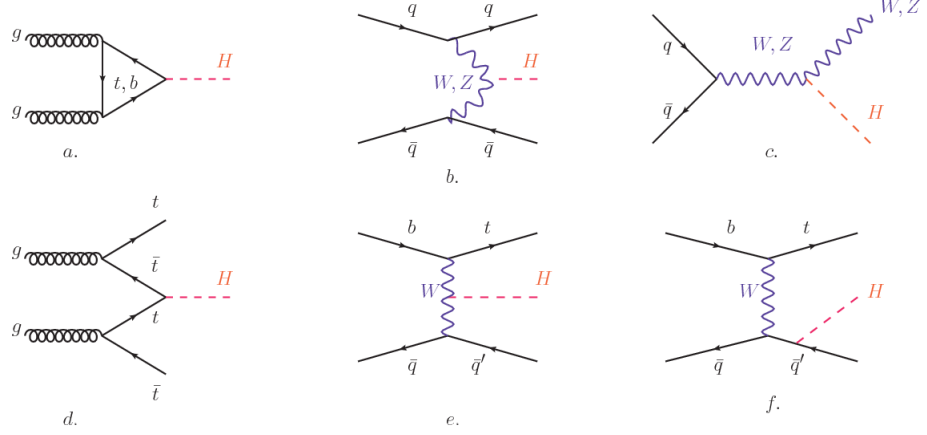


Figure 2.11: Main Higgs production mechanism Feynman diagrams. a. gluon-gluon fusion, b. vector boson fusion (VBF), c. Higgs-strahlung, d. Associated production with a top or bottom quark pair, e-f. associated production with a single top quark.

731 Figure 2.11 shows the Feynman diagrams for the leading order (first order) Higgs
 732 production processes at LHC, while the cross section for Higgs production as a func-
 733 tion of the center of mass-energy (\sqrt{s}) for pp collisions is showed in figure 2.12 left.
 734 The tags NLO (next to leading order), NNLO (next to next to leading order) and
 735 N3LO (next to next to next to leading order) make reference to the order at which
 736 the perturbation series have been considered.

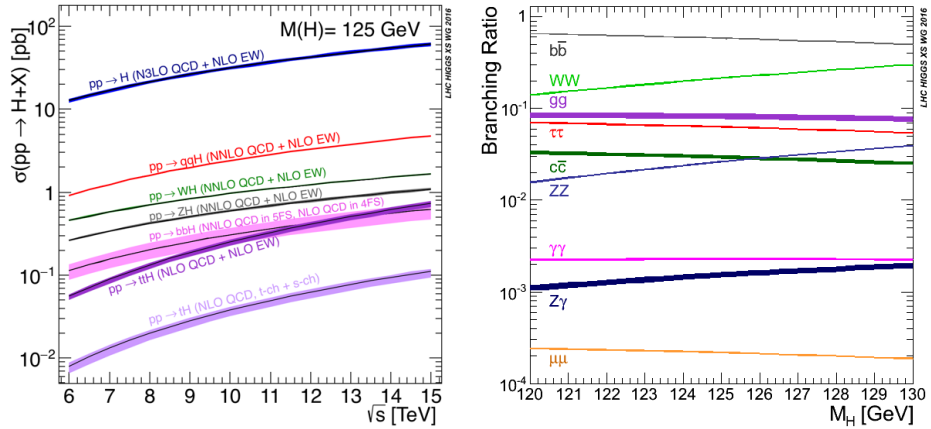


Figure 2.12: Higgs production cross sections (left) and decay branching ratios (right) for the main mechanisms. The VBF is indicated as qqH [42].

737 As shown in eqns 2.47, 2.51 and 2.55, the strength of the Higgs-fermion interaction

738 is proportional to the fermion mass while the strength of the Higgs-gauge boson
739 interaction is proportional to the square of the gauge boson mass, which implies
740 that the Higgs production and decay mechanisms are dominated by couplings $H -$
741 (W, Z, t, b, τ) .

742 The main production mechanism is the gluon fusion (figure 2.11a and $pp \rightarrow H$ in figure
743 2.12) given that gluons carry the highest fraction of momentum of the protons in pp
744 colliders. Since the Higgs boson does not couple to gluons, the mechanism proceeds
745 through the exchange of a virtual top-quark loop given that for it the coupling is
746 the biggest. Note that in this process, the Higgs boson is produced alone, which
747 makes this mechanism experimentally clean when combined with the two-photon or
748 the four-lepton decay channels (see section 2.3.7).

749 Vector boson fusion (figure 2.11b and $pp \rightarrow qqH$ in figure 2.12) has the second largest
750 production cross section. The scattering of two fermions is mediated by a weak
751 gauge boson which later emits a Higgs boson. In the final state, the two fermions
752 tend to be located in a particular region of the detector which is used as a signature
753 when analyzing the datasets provided by the experiments. More details about how
754 to identify events of interest in an analysis will be given in chapter 4.

755 The next production mechanism is Higgs-strahlung (figure 2.11c and $pp \rightarrow WH, pp \rightarrow$
756 ZH in figure 2.12) where two fermions annihilate to form a weak gauge boson. If the
757 initial fermions have enough energy, the emergent boson eventually will emit a Higgs
758 boson.

759 The associated production with a top or bottom quark pair and the associated pro-
760 duction with a single top quark (figure 2.11d-f and $pp \rightarrow bbH, pp \rightarrow t\bar{t}H, pp \rightarrow tH$
761 in figure 2.12) have a smaller cross section than the main three mechanisms above,
762 but they provide a good opportunity to test the Higgs-top coupling. The analysis
763 reported in this thesis is developed using these production mechanisms. A detailed

764 description of the tH mechanism will be given in section 2.4.

765 2.3.7 Higgs decay channels

766 When a particle can decay through several modes, also known as channels, the
 767 probability of decaying through a given channel is quantified by the “branching ratio
 768 (BR)” of the decay channel; thus, the BR is defined as the ratio of number of decays
 769 going through that given channel to the total number of decays. In regard to the
 770 Higgs boson decay, the BR can be predicted with accuracy once the Higgs mass is
 771 known [43, 44]. In figure 2.12 right, a plot of the BR as a function of the Higgs mass
 772 is presented. The largest predicted BR corresponds to the $b\bar{b}$ pair decay channel (see
 773 table 2.9).

Decay channel	Branching ratio	Rel. uncertainty
$H \rightarrow b\bar{b}$	5.84×10^{-1}	$+3.2\% - 3.3\%$
$H \rightarrow W^+W^-$	2.14×10^{-1}	$+4.3\% - 4.2\%$
$H \rightarrow \tau^+\tau^-$	6.27×10^{-2}	$+5.7\% - 5.7\%$
$H \rightarrow ZZ$	2.62×10^{-2}	$+4.3\% - 4.1\%$
$H \rightarrow \gamma\gamma$	2.27×10^{-3}	$+5.0\% - 4.9\%$
$H \rightarrow Z\gamma$	1.53×10^{-3}	$+9.0\% - 8.9\%$
$H \rightarrow \mu^+\mu^-$	2.18×10^{-4}	$+6.0\% - 5.9\%$

Table 2.9: Predicted branching ratios and the relative uncertainty for a SM Higgs boson with $m_H = 125\text{GeV}/c^2$. [21]

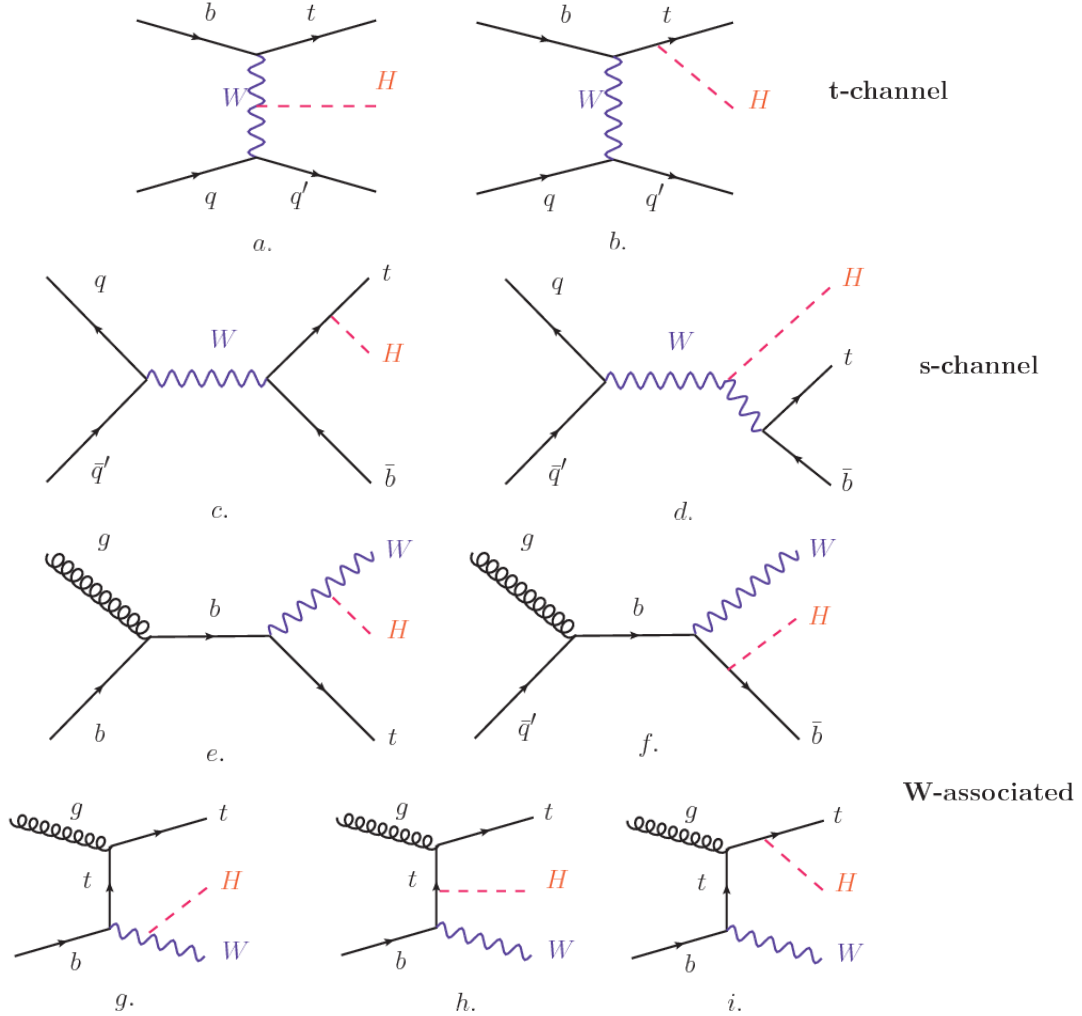


Figure 2.13: Associated higgs production mechanism Feynman diagrams. a.,b. t-channel (tHq), c.,d. s-channel ($tH\bar{b}$), e.-i. W-associated.

775 **2.4 Associated Production of Higgs Boson and**
 776 **Single Top Quark.**

777 Associated production of Higgs boson have been extensively studied [46–50]. While
 778 measurements of the main Higgs production mechanisms rates are sensitive to the
 779 strength of the Higgs coupling to W boson or top quark, they are not sensitive to the
 780 relative sign between the two couplings. In this thesis, the Higgs boson production

781 mechanism explored is the associated production with a single top quark (*th*) which
 782 offers sensitiveness to the relative sign of the Higgs couplings to W boson and to top
 783 quark. The description given here is based on the reference [48]

784

785 A process where two incoming particles interact and produce a final state with two
 786 particles can proceed in three ways also called channels (see, for instance, figure 2.13
 787 ommiting the red line). The t-channel represents processes where an intermediate
 788 particle is emitted by one of the incoming particles and absorbed by the other. The
 789 s-channel represent processes where the two incoming particles merge into an inter-
 790 mediate particle which eventually will split into the particles in the final state. The
 791 third channel, u-channel, is similar to the t-channel but the two outgoing particles
 792 interchange their roles.

793

794 The *th* production where Higgs boson can be radiated either from the top quark or
 795 from the W boson is represented by the leading order Feynman diagrams in figure
 796 2.13. The cross section for the *th* process is calculated, as usual, summing over
 797 the contributions from the different feynman diagrams; therefore it depends on the
 798 interference between the contributions. In the SM, the interference for t-channel (tHq
 799 process) and W-associated (tHW process) production is destructive [46] resulting in
 800 the small cross sections presented in table 2.10.

tH production channel	Cross section (fb)
t-channel ($pp \rightarrow tHq$)	$70.79^{+2.99}_{-4.80}$
W-associated ($pp \rightarrow tHW$)	$15.61^{+0.83}_{-1.04}$
s-channel($pp \rightarrow tHb$)	$2.87^{+0.09}_{-0.08}$

Table 2.10: Predicted SM cross sections for *tH* production at $\sqrt{s} = 13$ TeV [51,52].

801

802 While the s-channel contribution can be neglected, it will be shown that a deviation
 803 from the SM destructive interference would result in an enhancement of the th cross
 804 section compared to that in SM, which could be used to get information about the
 805 sign of the Higgs-top coupling [48, 49]. In order to describe th production processes,
 806 Feynman diagram 2.13b will be considered; there, the W boson is radiated by a
 807 quark in the proton and eventually it will interact with the b quark. In the high
 808 energy regime, the effective W approximation [53] allows to describe the process as
 809 the emmision of an approximately on-shell W and its hard scattering with the b
 810 quark; i.e. $Wb \rightarrow th$. The scattering amplitude for the process is given by

$$\mathcal{A} = \frac{g}{\sqrt{2}} \left[(C_t - C_V) \frac{m_t \sqrt{s}}{m_W v} A \left(\frac{t}{s}, \varphi; \xi_t, \xi_b \right) + \left(C_V \frac{2m_W}{v} \frac{s}{t} + (2C_t - C_V) \frac{m_t^2}{m_W v} \right) B \left(\frac{t}{s}, \varphi; \xi_t, \xi_b \right) \right], \quad (2.57)$$

811 where $C_V \equiv g_{HVV}/g_{HVV}^{SM}$ and $C_t \equiv g_{Ht}/g_{Ht}^{SM} = y_t/y_t^{SM}$ are scaling factors that quan-
 812 tify possible deviations of the couplings, Higgs-Vector boson (H-W) and Higgs-top
 813 (H-t) respectively, from the SM couplings; $s = (p_W + p_b)^2$, $t = (p_W - p_H)^2$, φ is the
 814 Higgs azimuthal angle around the z axis taken parallel to the direction of motion of
 815 the incoming W; A and B are funtions describing the weak interaction in terms of
 816 the chiral states of the quarks b and t. Terms that vanish in the high energy limit
 817 have been neglected as well as the Higgs and b quark masses⁹.

818 The scattering amplitude grows with energy like \sqrt{s} for $C_V \neq C_t$, in contract to
 819 the SM ($C_t = C_V = 1$) where the first term in 2.57 cancels out and the amplitude
 820 is constant for large s; therefore, a deviation from the SM predictions represent an
 821 enhancement in the tHq cross section. In particular, for a SM H-W coupling and
 822 a H-t coupling of inverted sigh with respect to the SM ($C_V = -C_t = 1$) the tHq

⁹ A detailed explanation of the structure and approximations used to derive \mathcal{A} can be fount in reference [48]

cross section is enhanced by a factor greater 10 as seen in the figure 2.14 taken from reference [48]; reference [54] have reported similar enhancement results.

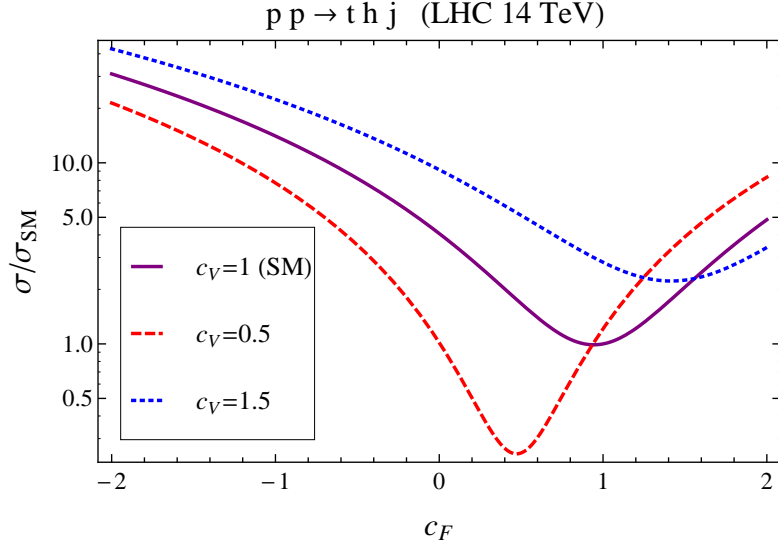


Figure 2.14: Cross section for tHq process as a function of C_t , normalized to the SM, for three values of C_V . In the plot C_f refers to the Higgs-fermion coupling which is dominated by the H-t coupling C_t . Solid, dashed and dotted lines correspond to $C_V = 1, 0.5, 1.5$ respectively. Note that for the SM ($C_V = C_t = 1$), the destructive effect of the interference is maximal.

A similar analysis is valid for the W-associated channel but, in that case, the interference is more complicated since there are more than two contributions and an additional interference with the production of Higgs boson and a top pair process($t\bar{t}H$). The calculations are made using the so-called Diagram Removal (DR) technique where interfering diagrams are removed (or added) from the calculations in order to evaluate the impact of the removed contributions. DR1 was defined to neglect $t\bar{t}H$ interference while DR2 was defined to take $t\bar{t}H$ interference into account [55]. As shown in figure 2.15, the tHW cross section is enhanced from about 15 fb (SM: $\kappa_{Htt} = 1$) to about 150 fb ($\kappa_{Htt} = -1$). Differences between curves for DR1 and DR2 help to gauge the impact of the interference with $t\bar{t}H$.

Results of the calculations of the tHq and tHW cross sections at $\sqrt{s} = 13$ TeV can be

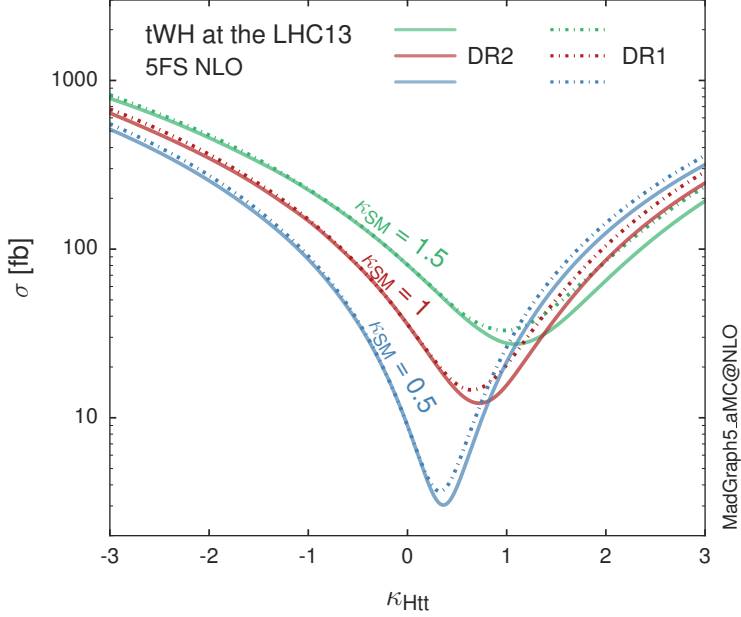


Figure 2.15: Cross section for tHW process as a function of κ_{Htt} , for three values of κ_{SSM} at $\sqrt{s} = 13$ TeV. $\kappa_{Htt}^2 = \sigma_{Htt}/\sigma_{Htt}^{SM}$ is a simple rescaling of the SM Higgs interactions.

836 found in reference [56] and a summary of the results is presented in table 2.11.

837

838 2.5 The CP-mixing in tH processes

839 In addition to the sensitivity to sign of the H-t coupling, tHq and tHW processes have
 840 been proposed as a tool to investigate the possibility of a H-t coupling that does not
 841 conserve CP [50, 55, 57]. Current experimental results are consistent with SM H-V
 842 and H-t couplings; however, negative H-t coupling is not excluded completely [60].

843

844 In this thesis, the sensitivity of th processes to CP-mixing is also studied in the
 845 effective field theory framework and based in references [50, 55]; a generic particle
 846 (X_0) of spin-0 and a general CP violating interaction with the top quark, can couples

	\sqrt{s} TeV	$C_t = 1$	$C_t = -1$
$\sigma^{LO}(tHq)(\text{fb})$ [48]	8	≈ 17.4	≈ 252.7
	14	≈ 80.4	≈ 1042
$\sigma^{NLO}(tHq)(\text{fb})$ [48]	8	$18.28^{+0.42}_{-0.38}$	$233.8^{+4.6}_{-0.0}$
	14	$88.2^{+1.7}_{-0.0}$	$982.8^{+28}_{-0.0}$
$\sigma^{LO}(tHq)(\text{fb})$ [54]	14	≈ 71.8	≈ 893
$\sigma^{LO}(tHW)(\text{fb})$ [54]	14	≈ 16.0	≈ 139
$\sigma^{NLO}(tHq)(\text{fb})$ [56]	8	$18.69^{+8.62\%}_{-17.13\%}$	-
	13	$74.25^{+7.48\%}_{-15.35\%}$	$848^{+7.37\%}_{-13.70\%}$
	14	$90.10^{+7.34\%}_{-15.13\%}$	$1011^{+7.24\%}_{-13.39\%}$
$\sigma^{LO}(tHW)(\text{fb})$ [55]	13	$15.77^{+15.91\%}_{-15.76\%}$	-
$\sigma^{NLO}DR1(tHW)(\text{fb})$ [55]	13	$21.72^{+6.52\%}_{-5.24\%}$	≈ 150
$\sigma^{NLO}DR2(tHW)(\text{fb})$ [55]	13	$16.28^{+7.34\%}_{-15.13\%}$	≈ 150

Table 2.11: Predicted enhancement of the tHq and tHW cross sections at LHC for $C_V = 1$ and $C_t = \pm 1$ at LO and NLO; the cross section enhancement of more than a factor of 10 is due to the flippling in the sign of the H-t coupling with respect to the SM one.

847 to scalar and pseudoscalar fermionic densities. The H-W interaction is assumed to
 848 be SM-like. The Lagrangian modeling the H-t interaction is given by

$$\mathcal{L}_0^t = -\bar{\psi}_t (c_\alpha \kappa_{Htt} g_{Htt} + i s_\alpha \kappa_{Att} g_{Att} \gamma_5) \psi_t X_0, \quad (2.58)$$

849 where α is the CP-mixing phase, $c_\alpha \equiv \cos \alpha$ and $s_\alpha \equiv \sin \alpha$, κ_{Htt} and κ_{Att} are real
 850 dimensionless rescaling parameters¹⁰, $g_{Htt} = g_{Att} = m_t/v = y_t/\sqrt{2}$ and $v \sim 246$ GeV
 851 is the Higgs vacuum expectation value. In this parametrization, it is easy to recover
 852 three special cases

853 • CP-even coupling $\rightarrow \alpha = 0^\circ$

854 • CP-odd coupling $\rightarrow \alpha = 90^\circ$

855 • SM coupling $\rightarrow \alpha = 0^\circ$ and $\kappa_{Htt} = 1$

¹⁰ analog to C_t and C_V

856 The loop induced X_0 coupling to gluons can also be described in terms of the
 857 parametrization above, according to

$$\mathcal{L}_0^g = -\frac{1}{4} \left(c_\alpha \kappa_{Hgg} g_{Hgg} G_{\mu\nu}^a G^{a,\mu\nu} + s_\alpha \kappa_{Agg} g_{Agg} G_{\mu\nu}^a \tilde{G}^{a,\mu\nu} \right) X_0. \quad (2.59)$$

858 where $g_{Hgg} = -\alpha_s/3\pi v$ and $g_{Agg} = \alpha_s/2\pi v$. Under the assumption that the top quark
 859 dominates the gluon-fusion process at LHC energies, $\kappa_{Hgg} \rightarrow \kappa_{Htt}$ and $\kappa_{Agg} \rightarrow \kappa_{Att}$,
 860 so that the ratio between the gluon-gluon fusion cross section for X_0 and for the SM
 861 Higgs prediction can be written as

$$\frac{\sigma_{NLO}^{gg \rightarrow X_0}}{\sigma_{NLO,SM}^{gg \rightarrow H}} = c_\alpha^2 \kappa_{Htt}^2 + s_\alpha^2 \left(\kappa_{Att} \frac{g_{Agg}}{g_{Hgg}} \right)^2. \quad (2.60)$$

862 If the rescaling parameters are set to

$$\kappa_{Htt} = 1, \quad \kappa_{Att} = \left| \frac{g_{Hgg}}{g_{Agg}} \right| = \frac{2}{3}. \quad (2.61)$$

863 the gluon-fusion SM cross section is reproduced for every value of the CP-mixing
 864 angle α ; therefore, by imposing that condition to the Lagrangian density 2.58, the
 865 CP-mixing angle is not constrained by current data. Figure 2.16 shows the NLO cross
 866 sections for t-channel tX_0 (blue) and $t\bar{t}X_0$ (red) associated production processes as
 867 a function of the CP-mixing angle α . X_0 is a generic spin-0 particle with top quark
 868 CP-violating coupling. Rescaling factors κ_{Htt} and κ_{Att} have been set to reproduce
 869 the SM gluon-fusion cross sections.

870 It is interesting to notice that the tX_0 cross section is enhanced, by a factor of
 871 about 10, when a continuous rotation in the scalar-pseudoscalar plane is applied; this
 872 enhancement is similar to the enhancement produced when the H-t coupling is flipped
 873 in sign with respect to the SM ($y_t = -y_{t,SM}$ in the plot), as showed in section 2.4. In

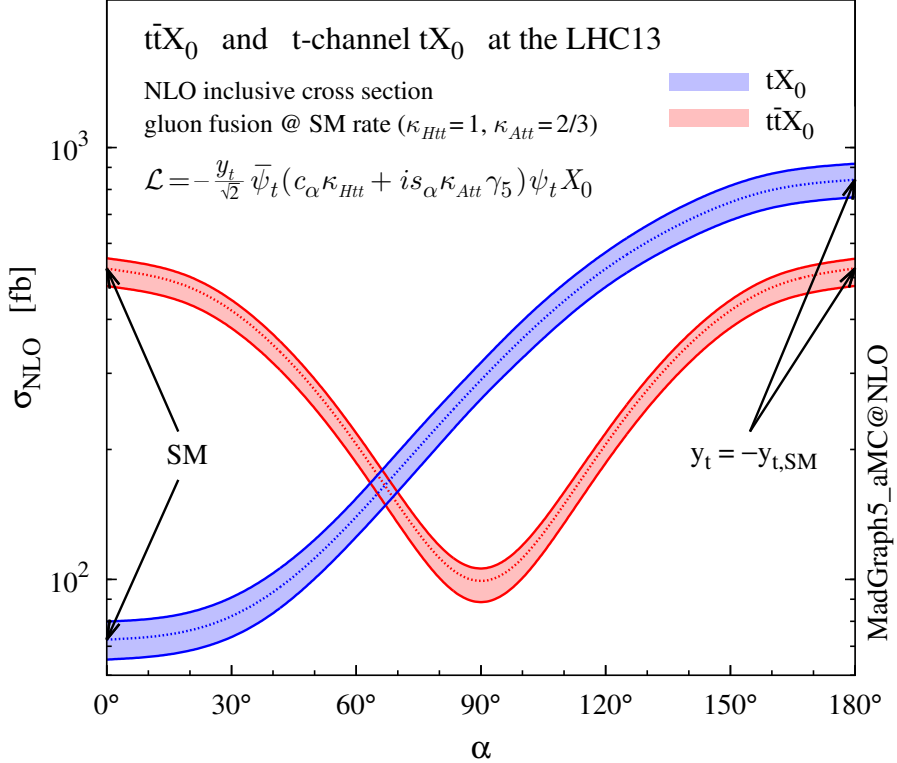


Figure 2.16: NLO cross sections for t-channel tX_0 (blue) and $t\bar{t}X_0$ (red) associated production processeses as a function of the CP-mixing angle α . X_0 is a generic spin-0 particle with top quark CP-violating coupling [50].

874 contrast, the degeneracy in the $t\bar{t}X_0$ cross section is still present given that it depends
 875 quadratically on the H-t coupling, but more insteresting is to notice that $t\bar{t}X_0$ cross
 876 section is exceeded by tX_0 cross section after $\alpha \sim 60^\circ$.

877 A similar parametrization can be used to investigate the tHW process sensitivity to
 878 CP-violating H-t coupling. As said in 2.4, the interference in the W-associated channel
 879 is more complicated because there are more than two contributions and also there is
 880 interference with the $t\bar{t}H$ production process.

881 Figure 2.17 shows the NLO cross sections for t-channel tX_0 (blue), $t\bar{t}X_0$ (red) asso-
 882 ciated production and for the combined $tWX_0 + t\bar{t}X_0 +$ interference (orange) as a
 883 function of the CP-mixing angle. It is clear that the effect of the interference in the

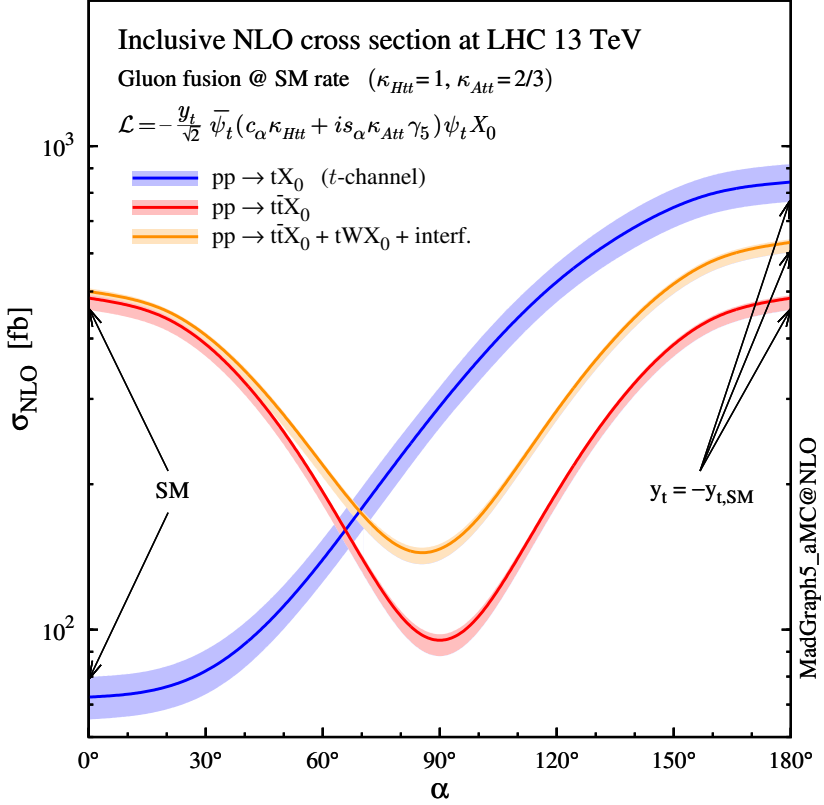


Figure 2.17: NLO cross sections for t-channel tX_0 (blue), $t\bar{t}X_0$ (red) associated production processes and combined $tWX_0 + t\bar{t}X_0$ (including interference) production as a function of the CP-mixing angle α [50].

combined case is the lifting of the degeneracy present in the $t\bar{t}X_0$ production. The constructive interference enhance the cross section from about 500 fb at SM ($\alpha = 0$) to about 600 fb ($\alpha = 180^\circ \rightarrow y_t = -y_{t,SM}$).
An analysis combining tHq and tHW proceses will be made in this thesis taking advantage of the sensitivity improvement.

⁸⁸⁹ **Chapter 3**

⁸⁹⁰ **The CMS experiment at the LHC**

⁸⁹¹ **3.1 Introduction**

⁸⁹² Located in the Swiss-French border, the European Council for Nuclear Research
⁸⁹³ (CERN) is the largest scientific organization leading the particle physics research.
⁸⁹⁴ About 13000 people in a broad range of fields including users, students, scientists,
⁸⁹⁵ engineers among others, contribute to the data taking and analysis, with the goal
⁸⁹⁶ of unveiling the secrets of the nature and revealing the fundamental structure of the
⁸⁹⁷ universe. CERN is also the home of the Large Hadron Collider (LHC), the largest
⁸⁹⁸ circular particle accelerator around the world, where protons (or heavy ions) travel-
⁸⁹⁹ ing close to the speed of light, are made to collide. These collisions open a window
⁹⁰⁰ to investigate how particles (and their constituents if they are composite) interact
⁹⁰¹ with each other, providing clues about the laws of the nature. This chapter present
⁹⁰² an overview of the LHC structure and operation; a brief mention of the four main
⁹⁰³ experiments that collect the information coming from the collisions is also included.
⁹⁰⁴ A more detailed description of the Compact Muon Solenoid (CMS) detector is offered,
⁹⁰⁵ given that the data used in this thesis have been taken with this detector.

906 3.2 The LHC

907 With 27 km of circumference, the LHC is currently the largest and most powerful
 908 accelerator in the world. It is installed in the same tunnel where the large Electron-
 909 Positron (LEP) collider was located, taking advantage of the existing infraestructure
 910 as shown in figure 3.1. Inside LHC, two particle beams, in two separated beam pipes
 911 kept at ultra high vacuum ($\sim 10^{-9}$ Pa) and traveling in counter-rotating trajectories,
 912 are accelerated to almost the speed of light. The beams intersect at four points where
 913 collisions take place. In 2008, the first set of collisions involved protons with center-
 914 of-mass energy (\sqrt{s}) of 7 TeV; the energy was increased to 8 TeV in 2012 and to 13
 915 TeV in 2015.

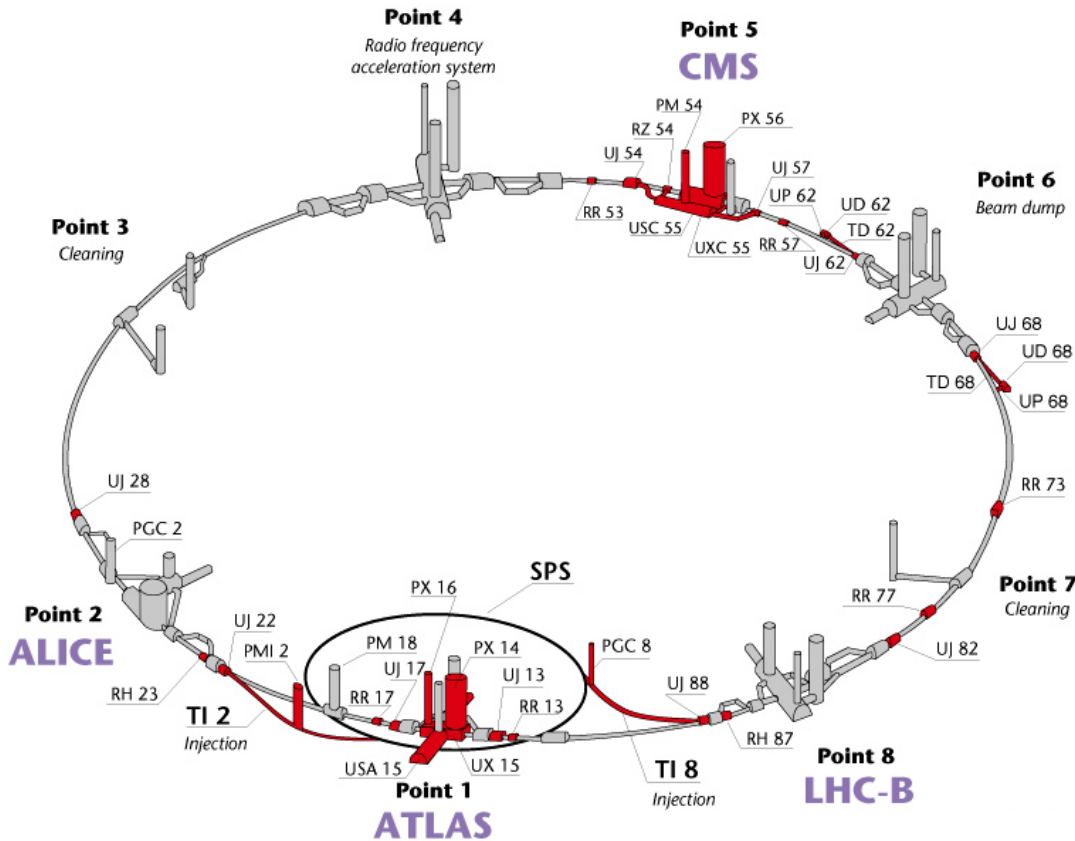


Figure 3.1: Layout of the LEP tunnel including LHC infrastructure additions (Red zones). [61]

916 The LHC is also the larger accelerator in the CERN's accelerator complex and is
 917 assisted by several successive accelerating stages before the particles are injected into
 918 the LHC ring where they reach their maximum energy(see figure 3.2). There are
 919 three run modes depending on the particles being accelerated

920 • Proton-Proton collisions (pp) for multiple physics experiments.

921 • Lead-Lead collisions (Pb-Pb) for heavy ion experiments.

922 • Proton-Lead collisions (p-Pb) for quark-gluon plasma experiments.

923 The acceleration process is depicted in figure 3.2. It starts with the collection of
 924 protons. Hydrogen atoms are taken from a bottle, containing hydrogen gas, injected
 925 in a metal cillinder and broken up into electrons and protons by an intense electric
 926 field¹. The resulting protons leave the metal cylinder towards the linear accelerator2
 927 (LINAC2) stage where the protons are accelerated until they reach 50 MeV energy.

928 Acceleration in the LINAC2 stage is conducted

929 and then injected into the proton synchrotron booster (BOOSTER) to reach 1.4
 930 GeV in energy. The next boost is provided at the proton synchrotron (PS) up to 26
 931 GeV, followed by the injection into the super proton synchrotron (SPS) where protons
 932 are accelerated to 450 GeV. Finally, protons are injected into the LHC where they
 933 are accelerated to the target energy of 6.5 TeV. In the Pb-Pb mode, the Lead ions are
 934 first accelerated in the LINAC3 and then passed as long pulses to the Low energy ion
 935 ring (LEIR) to be converted into short and dense bunches, each containing 7×10^7
 936 lead ions. LEIR accelerate the bunches from 4.2 MeV to 72 MeV. The ions are then
 937 passed to the PS to follow the rest of acceleration process up to 2.8TeV/n en the LHC
 938 ring.

¹ This very first stage is not represented in figure3.2

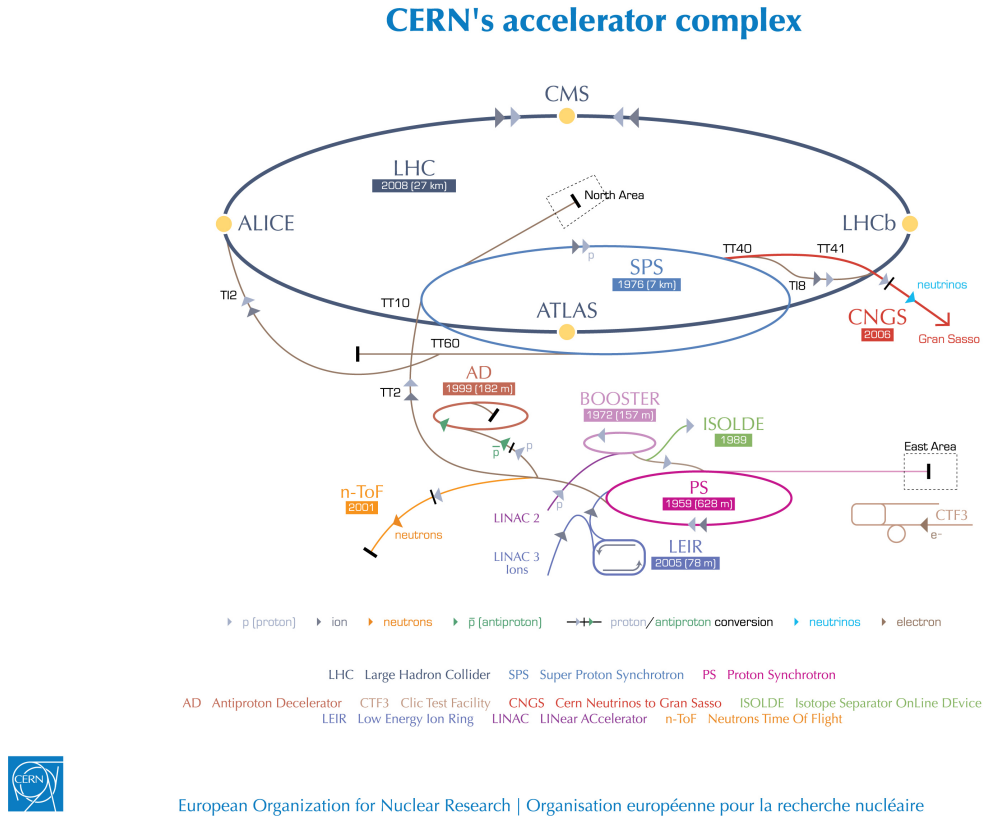


Figure 3.2: ref. C.Lefevre, “The CERN accelerator complex,” (2008). CERN-DI-0812015.

939 composed of superconducting magnets and accelerating structures (among other
 940 components)

941 The LHC is a circular accelerator of about 27 Km of circumference within the CERN
 942 As a The operation principle of LHC is based on the lorentz force that affects charged
 943 particles in motion within electric and magnetic fields.

944 In order to keep the protons in the circular trajectory carrying that amount of
 945 energy, strong magnetic fields are needed, bringing the superconductivity into scene.

946 The superconducting dipole magnets used in LHC are made of a NbTi alloy, capable
 947 of transporting currents of about 12000 A when cooled at a temperature below 2K by
 948 using liquid helium; that current generates a magnetic fields of 8.3 T. Figure 3.3 shows
 949 the transverse view of the LHC dipole magnets. Additionally, quadrupole magnets

950 are used to focus the beam and some other magnetic multipoles are used to correct
 951 effects generated by the interaction among protons in the beam as well as interactions
 952 within the beam pipe.

LHC DIPOLE : STANDARD CROSS-SECTION

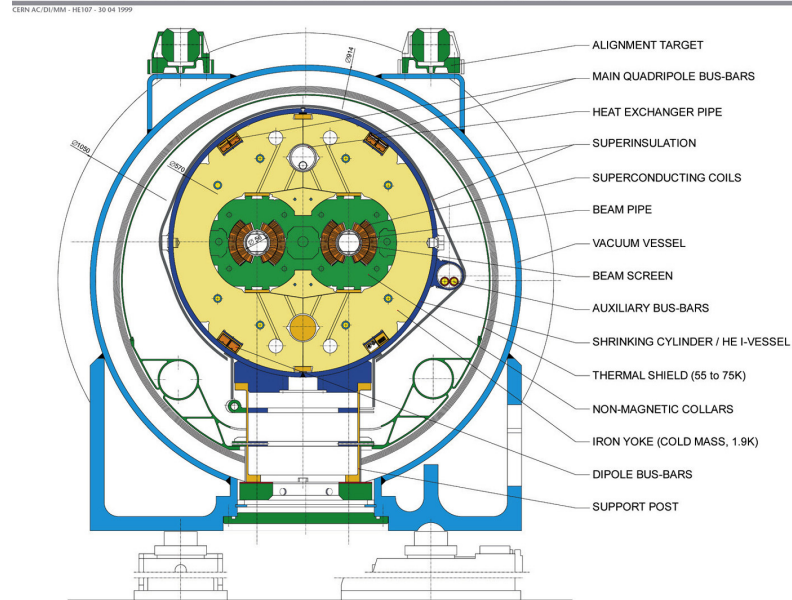


Figure 3.3: ref. ACTeam, “Diagram of an LHC dipole magnet. Schéma d’un aimant dipôle du LHC,” (1999). CERN-DI-9906025.

953 Regarding to the longitudinal acceleration of the protons, a system of 16 radio-
 954 frecuency cavities (RF) (8 per beam) is used to accelerate protons. Inside the cavities,
 955 the electromagnetic waves become resonant transferring the maximum energy to the
 956 particle flight through it. Cavities are cooled at 4.5 K. On LHC the RF oscillation
 957 frecuency is 400MHz and the protons are carefully timed so additionally to the ac-
 958 celeration effect the bunch structure of the beam is preserved. The Beam is made
 959 of 2808 “bunches” which are packages of 1.15×10^{11} protons ???. If LHC is at full
 960 energy, protons with the right energy does not feel any accelerating force but those
 961 with a different energy will be accelerated or decelerated to keep them in the bunch.
 962 The paths followed by particles during the acceleration process are shown in Figure

963 3.2.

964 Once the beams reach the desired energy, they are brought to cross each other
965 producing proton-proton collisions. The bunch crossing happens in precise places
966 where the LHC experiments are located. As seen in Figure ??, it was needed to
967 build the caverns for CMS and ATLAS as well as some additional facilities, but
968 most of the initial LEP infrastructure has been used to allocate additional collision
969 points. The highest luminosity is delivered at the CMS (point 5) and ATLAS (point
970 1) experiments, which are general purpose experiments, enabled to explore physics
971 in any of the collision modes. LHCb (point 8) experiment is optimized to explore
972 B-physics, while ALICE (point 2) is optimized for heavy ion collisions researches;
973 TOTEM (point 5) and LHCf (point 1) are dedicated to forward physics studies and
974 MoEDAL (point 8) is intended for monopoles or massive pseudo stable particles
975 studies.

976 **3.3 The CMS experiment**

977 The Compact Muon Solenoid (CMS) is a general purpose detector designed to conduct
978 research in a wide range of physics from standard model to new physics like extra
979 dimensions and dark matter. Located at the point 5 in the LHC layout as shown in
980 Figure ??, CMS is composed by several detection systems distributed in a cylindrical
981 structure where the main feature is a solenoid magnet made of superconducting cable
982 capable to generate a 3.8 T magnetic field. In total, CMS weight about 14000 tons
983 in a very compact 21.6 m long and 14.6 m diameter cylinder (include areference for
984 CMS TDR). It was built in 15 separated sections at the ground level and lowered
985 to the cavern individually to be assembled. Figure 3.4 show the layout of the CMS
986 detector (CMS TDR).

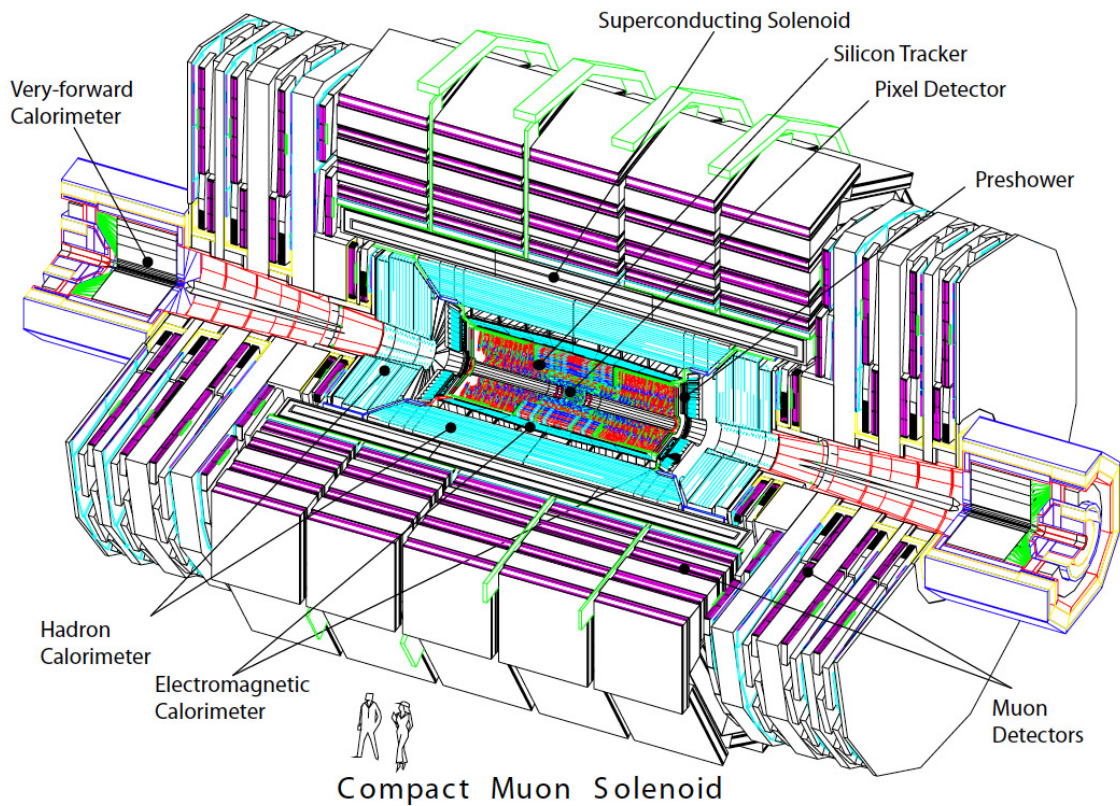


Figure 3.4: ref: CMS Collaboration, “Detector Drawings”, CMS-PHO-GEN-2012-002, <http://cds.cern.ch/record/1433717>, 2012.

987 **3.3.1 coordinate system**

988 **3.3.2 tracker- pixels and strips**

989 **3.3.3 calorimeters**

990 **3.3.4 magnet**

991 **3.3.5 muon system**

992 **3.3.6 trigger system - HLT- L1**

993 **3.3.7 computing model**

994 **3.4 Event generation simulation and
995 reconstruction**

996 **3.4.1 event generation**

997 **3.4.2 Hard scattering**

998 **3.4.3 parton shower**

999 **3.4.4 hadronization and decays**

1000 **3.4.5 underlying events and pileup**

1001 **3.4.6 MC - MadEvent, MadGraph and madgraphNLO,**
1002 **powheg, pythia, tauola**

1003 **3.4.7 detector simulation**

1004 **3.4.8 event reconstruction- particle flow algorithm,**
1005 **vertexing , muon reco, electron reco, photon and**

¹⁰¹⁴ **Chapter 4**

¹⁰¹⁵ **Search for production of a Higgs**
¹⁰¹⁶ **boson and a single top quark in**
¹⁰¹⁷ **multilepton final states in pp**
¹⁰¹⁸ **collisions at $\sqrt{s} = 13$ TeV**

¹⁰¹⁹ **4.1 Introduction**

¹⁰²⁰ Dont forget to mention previous constrains to ct check reference ?? and references
¹⁰²¹ <https://link.springer.com/content/pdf/10.1007%2FJHEP01>
¹⁰²² A. Azatov, R. Contino and J. Galloway, âIJModel-Independent Bounds on a
¹⁰²³ Light Higgs,â JHEP 1204 (2012) 127 [arXiv:1202.3415 [hep-ph]].
¹⁰²⁴ J. R. Espinosa, C. Grojean, M. Muhlleitner and M. Trott, âIJFingerprinting
¹⁰²⁵ Higgs Suspects at the LHC,â JHEP 1205 (2012) 097 [arXiv:1202.3697 [hep-ph]].
¹⁰²⁶ This chapter present the search for the associated production of a Higgs boson and
¹⁰²⁷ a single top quark events with three leptons in the final state, targeting Higgs decay

1028 modes to WW , ZZ , and $\tau\tau$. The analysis uses the 13 TeV dataset produced in 2016,
 1029 corresponding to an integrated luminosity of 35.9fb^{-1} . It is based on and expands
 1030 previous analyses at 8 TeV [62, 63] and searches for associated production of $t\bar{t}$ and
 1031 Higgs in the same channel [64], and complements searches in other decay channels
 1032 targeting $H \rightarrow b\bar{b}$ [65].

1033 As showed in section 2.4, the cross section of the associated production of a Higgs
 1034 boson and a single top quark (tHq) process is driven by a destructive interference of
 1035 two contributions (see Figure 4.1), where the Higgs couples to either the W boson or
 1036 the top quark. Any deviation from the standard model (SM) in the Higgs coupling
 1037 structure could therefore lead to a large enhancement of the cross section, making
 1038 this analysis sensitive to such deviations. A second process, where the Higgs and
 1039 top quark are accompanied by a W boson (tHW) has similar behavior, albeit with a
 1040 weaker interference pattern.

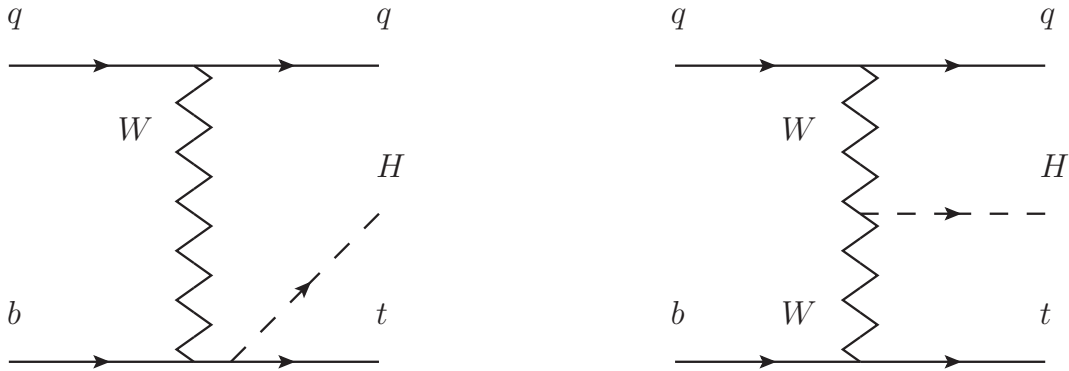


Figure 4.1: The two leading-order diagrams of tHq production.

1041 We selects events with three leptons and a b tagged jet in the final state. The tHq
 1042 signal contribution is then determined in a fit of the observed data to two multivariate
 1043 classifier outputs, each trained to discriminate against one of the two dominant back-
 1044 grounds of events with non-prompt leptons from $t\bar{t}$ and of associated production of $t\bar{t}$

1045 and vector bosons ($t\bar{t}W$, $t\bar{t}Z$). The fit result is then used to set an upper limit on the
 1046 combined $t\bar{t}H$, tHq and tHW production cross section, as a function of the relative
 1047 coupling strengths of Higgs and top quark and Higgs and W boson, respectively.

1048 4.2 Data and MC Samples

1049 The data considered in this analysis were collected by the CMS experiment dur-
 1050 ing 2016 and correspond to a total integrated luminosity of 35.9fb^{-1} . Only periods
 1051 when the CMS magnet was on were considered when selecting the data samples, that
 1052 corresponds to the 23 Sep 2016 (Run B to G) and PromptReco (Run H) versions
 1053 of the datasets. The MC samples used in this analysis correspond to the RunI-
 1054 ISummer16MiniAODv2 campaign produced with CMSSW 80X. The two signal sam-
 1055 ples (for tHq and tHW) were produced with MG5_aMC@NLO (version 5.222), in
 1056 leading-order mode, and are normalized to next-to-leading-order cross sections,
 1057 see Tab. 4.1. Each sample is generated with a set of event weights corresponding to
 1058 different values of κ_t and κ_V couplings as shown in Tab. 4.2.

1059 4.2.1 Full 2016 dataset and MC samples

Sample	σ [pb]	BF
/THQ_Hincl_13TeV-madgraph-pythia8_TuneCUETP8M1/	0.7927	0.324
/THW_Hincl_13TeV-madgraph-pythia8_TuneCUETP8M1/	0.1472	1.0

Table 4.1: Signal samples and their cross section and branching fraction used in this analysis. See Ref. [66] for more details.

1060 Different MC generators were used to generate the background processes. The
 1061 dominant sources ($t\bar{t}$, $t\bar{t}W$, $t\bar{t}Z$, $t\bar{t}H$) were produced using AMC@NLO interfaced
 1062 to PYTHIA8, and are scaled to NLO cross sections. Other processes are simulated

		<i>tHq</i>		<i>tHW</i>		
κ_V	κ_t	sum of weights	cross section [pb]	sum of weights	cross section [pb]	LHE weights
1.0	-3.0	35.700022	2.991	11.030445	0.6409	LHEweight_wgt[446]
1.0	-2.0	20.124298	1.706	5.967205	0.3458	LHEweight_wgt[447]
1.0	-1.5	14.043198	1.205	4.029093	0.2353	LHEweight_wgt[448]
1.0	-1.25	11.429338	0.9869	3.208415	0.1876	LHEweight_wgt[449]
1.0	-1.0		0.7927		0.1472	
1.0	-0.75	7.054998	0.6212	1.863811	0.1102	LHEweight_wgt[450]
1.0	-0.5	5.294518	0.4723	1.339886	0.07979	LHEweight_wgt[451]
1.0	-0.25	3.818499	0.3505	0.914880	0.05518	LHEweight_wgt[452]
1.0	0.0	2.627360	0.2482	0.588902	0.03881	LHEweight_wgt[453]
1.0	0.25	1.719841	0.1694	0.361621	0.02226	LHEweight_wgt[454]
1.0	0.5	1.097202	0.1133	0.233368	0.01444	LHEweight_wgt[455]
1.0	0.75	0.759024	0.08059	0.204034	0.01222	LHEweight_wgt[456]
1.0	1.0	0.705305	0.07096	0.273617	0.01561	LHEweight_wgt[457]
1.0	1.25	0.936047	0.0839	0.442119	0.02481	LHEweight_wgt[458]
1.0	1.5	1.451249	0.1199	0.709538	0.03935	LHEweight_wgt[459]
1.0	2.0	3.335034	0.2602	1.541132	0.08605	LHEweight_wgt[460]
1.0	3.0	10.516125	0.8210	4.391335	0.2465	LHEweight_wgt[461]
1.5	-3.0	45.281492	3.845	13.426212	0.7825	LHEweight_wgt[462]
1.5	-2.0	27.606715	2.371	7.809713	0.4574	LHEweight_wgt[463]
1.5	-1.5	20.476088	1.784	5.594971	0.3290	LHEweight_wgt[464]
1.5	-1.25	17.337465	1.518	4.635978	0.2749	LHEweight_wgt[465]
1.5	-1.0	14.483302	1.287	3.775902	0.2244	LHEweight_wgt[466]
1.5	-0.75	11.913599	1.067	3.014744	0.1799	LHEweight_wgt[467]
1.5	-0.5	9.628357	0.874	2.352505	0.1410	LHEweight_wgt[468]
1.5	-0.25	7.627574	0.702	1.789184	0.1081	LHEweight_wgt[469]
1.5	0.0	5.911882	0.5577	1.324946	0.08056	LHEweight_wgt[470]
1.5	0.25	4.479390	0.4365	0.959295	0.05893	LHEweight_wgt[471]
1.5	0.5	3.331988	0.3343	0.692727	0.04277	LHEweight_wgt[472]
1.5	0.75	2.469046	0.2558	0.525078	0.03263	LHEweight_wgt[473]
1.5	1.0	1.890565	0.2003	0.456347	0.02768	LHEweight_wgt[474]
1.5	1.25	1.596544	0.1689	0.486534	0.02864	LHEweight_wgt[475]
1.5	1.5	1.586983	0.1594	0.615638	0.03509	LHEweight_wgt[476]
1.5	2.0	2.421241	0.2105	1.170602	0.06515	LHEweight_wgt[477]
1.5	3.0	7.503280	0.5889	3.467546	0.1930	LHEweight_wgt[478]
0.5	-3.0	27.432685	2.260	8.929074	0.5136	LHEweight_wgt[479]
0.5	-2.0	13.956013	1.160	4.419093	0.2547	LHEweight_wgt[480]
0.5	-1.5	8.924438	0.7478	2.757611	0.1591	LHEweight_wgt[481]
0.5	-1.25	6.835341	0.5726	2.075247	0.1204	LHEweight_wgt[482]
0.5	-1.0	5.030704	0.4273	1.491801	0.08696	LHEweight_wgt[483]
0.5	-0.75	3.510528	0.2999	1.007273	0.05885	LHEweight_wgt[484]
0.5	-0.5	2.274811	0.1982	0.621663	0.03658	LHEweight_wgt[485]
0.5	-0.25	1.323555	0.1189	0.334972	0.01996	LHEweight_wgt[486]
0.5	0.0	0.656969	0.06223	0.147253	0.008986	LHEweight_wgt[487]
0.5	0.25	0.274423	0.02830	0.058342	0.003608	LHEweight_wgt[488]
0.5	0.5	0.176548	0.01778	0.068404	0.003902	LHEweight_wgt[489]
0.5	0.75	0.363132	0.03008	0.177385	0.009854	LHEweight_wgt[490]
0.5	1.0	0.834177	0.06550	0.385283	0.02145	LHEweight_wgt[491]
0.5	1.25	1.589682	0.1241	0.692099	0.03848	LHEweight_wgt[492]
0.5	1.5	2.629647	0.2047	1.097834	0.06136	LHEweight_wgt[493]
0.5	2.0	5.562958	0.4358	2.206057	0.1246	LHEweight_wgt[494]
0.5	3.0	14.843102	1.177	5.609519	0.3172	LHEweight_wgt[495]

Table 4.2: κ_V and κ_t combinations generated for the two signal samples and their NLO cross sections. The *tHq* cross section is multiplied by the branching fraction of the enforced leptonic decay of the top quark (0.324). See also Ref. [66].

Sample	σ [pb]
TTWJetsToLNu_TuneCUETP8M1_13TeV-amcatnloFXFX-madspin-pythia8	0.2043
TTZToLLNuNu_M-10_TuneCUETP8M1_13TeV-amcatnlo-pythia8	0.2529
ttHJetToNonbb_M125_13TeV_amcatnloFXFX_madspin_pythia8_mWCutfix	0.2151
/store/cmst3/group/susy/gpetrucc/13TeV/u/TTLL_m1to10_LO_NoMS_for76X/	0.0283
WGToLNug_TuneCUETP8M1_13TeV-madgraphMLM-pythia8	585.8
ZGTo2LG_TuneCUETP8M1_13TeV-amcatnloFXFX-pythia8	131.3
TGJets_TuneCUETP8M1_13TeV_amcatnlo_madspin_pythia8	2.967
TGJets_TuneCUETP8M1_13TeV_amcatnlo_madspin_pythia8	2.967
TTGJets_TuneCUETP8M1_13TeV-amcatnloFXFX-madspin-pythia8	3.697
WpWpJJ_EWK-QCD_TuneCUETP8M1_13TeV-madgraph-pythia8	0.03711
ZZZ_TuneCUETP8M1_13TeV-amcatnlo-pythia8	0.01398
WWZ_TuneCUETP8M1_13TeV-amcatnlo-pythia8	0.1651
WZZ_TuneCUETP8M1_13TeV-amcatnlo-pythia8	0.05565
WW_DoubleScattering_13TeV-pythia8	1.64
tZq_1l_4f_13TeV-amcatnlo-pythia8_TuneCUETP8M1	0.0758
ST_tW1l_5f_L0_13TeV-MadGraph-pythia8	0.01123
TTTT_TuneCUETP8M1_13TeV-amcatnlo-pythia8	0.009103
WZTo3LNu_TuneCUETP8M1_13TeV-powheg-pythia8	4.4296
ZZTo4L_13TeV_powheg_pythia8	1.256
TTJets_SingleLeptFromTbar_TuneCUETP8M1_13TeV-madgraphMLM-pythia8	182.1754
TTJets_SingleLeptFromT_TuneCUETP8M1_13TeV-madgraphMLM-pythia8	182.1754
TTJets_DiLept_TuneCUETP8M1_13TeV-madgraphMLM-pythia8	87.3
DYJetsToLL_M-10to50_TuneCUETP8M1_13TeV-amcatnloFXFX-pythia8	18610
DYJetsToLL_M-50_TuneCUETP8M1_13TeV-madgraphMLM-pythia8	6024
WJetsToLNu_TuneCUETP8M1_13TeV-amcatnloFXFX-pythia8	61526.7
ST_tW_top_5f_inclusiveDecays_13TeV-powheg-pythia8_TuneCUETP8M1	35.6
ST_tW_antitop_5f_inclusiveDecays_13TeV-powheg-pythia8_TuneCUETP8M1	35.6
ST_t-channel_4f_leptonDecays_13TeV-amcatnlo-pythia8_TuneCUETP8M1	70.3144
ST_t-channel_antitop_4f_leptonDecays_13TeV-powheg-pythia8_TuneCUETP8M1	26.2278
ST_s-channel_4f_leptonDecays_13TeV-amcatnlo-pythia8_TuneCUETP8M1	3.68064
WWTo2L2Nu_13TeV-powheg	10.481

Table 4.3: List of background samples used in this analysis (CMSSW 80X). In the first section of the table are listed the samples of the processes for which we use the simulation to extract the final yields and shapes, in the second section the samples of the processes we will estimate from data. The MC simulation is used to design the data driven methods and derive the associated systematics.

Sample	σ [pb]
ttWJets_13TeV_madgraphMLM	0.6105
ttZJets_13TeV_madgraphMLM	0.5297/0.692

Table 4.4: Leading-order $t\bar{t}W$ and $t\bar{t}Z$ samples used in the signal BDT training.

1063 using POWHEG interfaced to PYTHIA, or bare PYTHIA (see table 4.3 and [64]
1064 for more details).

Three lepton and Four lepton
HLT_DiMu9_Ele9_CaloIdL_TrackIdL_v*
HLT_Mu8_DiEle12_CaloIdL_TrackIdL_v*
HLT_TripleMu_12_10_5_v*
HLT_Ele16_Ele12_Ele8_CaloIdL_TrackIdL_v*
HLT_Mu23_TrkIsoVVL_Ele8_CaloIdL_TrackIdL_IsoVL_v*
HLT_Mu23_TrkIsoVVL_Ele8_CaloIdL_TrackIdL_IsoVL_DZ_v*
HLT_Mu8_TrkIsoVVL_Ele23_CaloIdL_TrackIdL_IsoVL_v*
HLT_Mu8_TrkIsoVVL_Ele23_CaloIdL_TrackIdL_IsoVL_DZ_v*
HLT_Ele23_Ele12_CaloIdL_TrackIdL_IsoVL_DZ_v*
HLT_Mu17_TrkIsoVVL_Mu8_TrkIsoVVL_DZ_v*
HLT_Mu17_TrkIsoVVL_TkMu8_TrkIsoVVL_DZ_v*
HLT_IsoMu22_v*
HLT_IsoTkMu22_v*
HLT_IsoMu22_eta2p1_v*
HLT_IsoTkMu22_eta2p1_v*
HLT_IsoMu24_v*
HLT_IsoTkMu24_v*
HLT_Ele27_WPTight_Gsf_v*
HLT_Ele25_eta2p1_WPTight_Gsf_v*
HLT_Ele27_eta2p1_WPLoose_Gsf_v*

Table 4.5: Table of high-level triggers that we consider in the analysis.

1065 4.2.2 Triggers

1066 We consider online-reconstructed events triggered by one, two, or three leptons.
 1067 Single-lepton triggers are included to boost the acceptance of events where the p_T of
 1068 the sub-leading lepton falls below the threshold of the double-lepton triggers. Ad-
 1069 ditionally, by including double-lepton triggers in the ≥ 3 lepton category, as well
 1070 as single-lepton triggers in all categories, we increase the efficiency, considering the
 1071 logical “or” of the trigger decisions of all the individual triggers in a given category.
 1072 Tab. 4.5 shows the lowest-threshold non-prescaled triggers present in the High-Level
 1073 Trigger (HLT) menus for both Monte-Carlo and data in 2016.

1074 4.2.2.1 Trigger efficiency scale factors

1075 The efficiency of events to pass the trigger is measured in simulation (trivially using
 1076 generator information) and in the data (using event collected by an uncorrelated

Category	Scale Factor
ee	1.01 ± 0.02
e μ	1.01 ± 0.01
$\mu\mu$	1.00 ± 0.01
3l	1.00 ± 0.03

Table 4.6: Trigger efficiency scale factors and associated uncertainties, shown here rounded to the nearest percent.

1077 MET trigger). Small differences between the data and MC efficiencies are corrected
 1078 by applying scale factors as shown in Tab. 4.6. The exact procedure and control plots
 1079 are documented in [67] for the current analysis.

1080 4.3 Object Identification and event selection

1081 4.3.1 Jets and b tagging

1082 The analysis uses anti- k_t (0.4) particle-flow (PF) jets, corrected for charged hadrons
 1083 not coming from the primary vertex (charged hadron subtraction), and having jet
 1084 energy corrections (`Summer16_23Sep2016V3`) applied as a function of the jet E_T and
 1085 η . Jets are only considered if they have a transverse energy above 25GeV.

1086 In addition, they are required to be separated from any lepton candidates passing
 1087 the fakeable object selections (see Tables 4.7 and 4.8) by $\Delta R > 0.4$.

1088 The loose and medium working points of the CSV b-tagging algorithm are used to
 1089 identify b jets. Data/simulation differences in the b tagging performance are corrected
 1090 by applying per-jet weights to the simulation, dependent on the jet p_T , eta, b tagging
 1091 discriminator, and flavor (from simulation truth) [68]. The per-event weight is taken
 1092 as the product of the per-jet weights, including those of the jets associated to the
 1093 leptons. More details can be found in the corresponding $t\bar{t}H$ documentation [64, 67].

1094 **4.3.2 Lepton selection**

Cut	Loose	Fakeable object	Tight
$ \eta < 2.4$	✓	✓	✓
p_T	$> 5\text{GeV}$	$> 15\text{GeV}$	$> 15\text{GeV}$
$ d_{xy} < 0.05 \text{ (cm)}$	✓	✓	✓
$ d_z < 0.1 \text{ (cm)}$	✓	✓	✓
$\text{SIP}_{3D} < 8$	✓	✓	✓
$I_{\text{mini}} < 0.4$	✓	✓	✓
is Loose Muon	✓	✓	✓
jet CSV	—	< 0.8484	< 0.8484
is Medium Muon	—	—	✓
tight-charge	—	—	✓
lepMVA > 0.90	—	—	✓

Table 4.7: Requirements on each of the three muon selections. In the cases where the cut values change between the selections, those values are listed in the table. Otherwise, whether the cut is applied is indicated. For the two p_T^{ratio} and CSV rows, the cuts marked with a † are applied to leptons that fail the lepton MVA cut, while the loose cut value is applied to those that pass the lepton MVA cut.

1095 The lepton reconstruction and selection is identical to that used in the $t\bar{t}H$ mul-
 1096 tilepton analysis, as documented in Refs. [64, 67]. For details on the reconstruction
 1097 algorithms, isolation, pileup mitigation, and a description of the lepton MVA discrim-
 1098 inator and validation plots thereof, we refer to that document since they are out of
 1099 the scope of this thesis. Three different selections are defined both for the electron
 1100 and muon object identification: the *Loose*, *Fakeable Object*, and *Tight* selection. As
 1101 described in more detail later, these are used for event level vetoes, the fake rate
 1102 estimation application region, and the final signal selection, respectively. The p_T of
 1103 fakeable objects is defined as $0.85 \times p_T(\text{jet})$, where the jet is the one associated to the
 1104 lepton object. This mitigates the dependence of the fake rate on the momentum of
 1105 the fakeable object and thereby improves the precision of the method.

1106 Tables 4.7 and 4.8 list the full criteria for the different selections of muons and
 1107 electrons.

Cut	Loose	Fakeable Object	Tight
$ \eta < 2.5$	✓	✓	✓
p_T	$> 7\text{GeV}$	$> 15\text{GeV}$	$> 15\text{GeV}$
$ d_{xy} < 0.05 \text{ (cm)}$	✓	✓	✓
$ d_z < 0.1 \text{ (cm)}$	✓	✓	✓
$\text{SIP}_{3D} < 8$	✓	✓	✓
$I_{\text{mini}} < 0.4$	✓	✓	✓
MVA ID $> (0.0, 0.0, 0.7)$	✓	✓	✓
$\sigma_{i\eta i\eta} < (0.011, 0.011, 0.030)$	—	✓	✓
$\text{H/E} < (0.10, 0.10, 0.07)$	—	✓	✓
$\Delta\eta_{in} < (0.01, 0.01, 0.008)$	—	✓	✓
$\Delta\phi_{in} < (0.04, 0.04, 0.07)$	—	✓	✓
$-0.05 < 1/E - 1/p < (0.010, 0.010, 0.005)$	—	✓	✓
p_T^{ratio}	—	$> 0.5 \dagger / -$	—
jet CSV	—	$< 0.3 \dagger / < 0.8484$	< 0.8484
tight-charge	—	—	✓
conversion rejection	—	—	✓
Number of missing hits	< 2	$== 0$	$== 0$
lepMVA > 0.90	—	—	✓

Table 4.8: Criteria for each of the three electron selections. In cases where the cut values change between selections, those values are listed in the table. Otherwise, whether the cut is applied is indicated. In some cases, the cut values change for different η ranges. These ranges are $0 < |\eta| < 0.8$, $0.8 < |\eta| < 1.479$, and $1.479 < |\eta| < 2.5$ and the respective cut values are given in the form (value₁, value₂, value₃).

4.3.3 Lepton selection efficiency

Efficiencies of reconstruction and selecting loose leptons are measured both for muons and electrons using a tag and probe method on both data and MC, using $Z \rightarrow \ell^+ \ell^-$. Corresponding scale factors are derived from the ratio of efficiencies and applied to the selected These. Events are produced for the leptonic SUSY analyses using equivalent lepton selections and recycled for the $t\bar{t}H$ analysis as well as for this analysis. The efficiencies of applying the tight selection as defined in Tables 4.7 and 4.8, on the loose leptons are determined again by using a tag and probe method on a sample of DY-enriched events. They are documented for the $t\bar{t}H$ analysis in Ref. [67] and are exactly equivalent for this analysis.

1118 4.4 Background predictions

1119 The modeling of reducible and irreducible backgrounds in this analysis uses the exact
 1120 methods, analysis code, and ROOT trees used for the $t\bar{t}H$ multilepton analysis. We
 1121 give a brief description of the methods and refer to the documentation of that analysis
 1122 in Refs. [64, 67] for any details.

1123 The backgrounds in three-lepton final states can be split in two broad categories:
 1124 irreducible backgrounds with genuine prompt leptons (i.e. from on-shell W and Z
 1125 boson decays); and reducible backgrounds where at least one of the leptons is “non-
 1126 prompt”, i.e. produced within a hadronic jet, either a genuine lepton from heavy
 1127 flavor decays, or simply mis-reconstructed jets.

1128 Irreducible backgrounds can be reliably estimated directly from Monte-Carlo sim-
 1129 ulated events, using higher-order cross sections or data control regions for the overall
 1130 normalization. This is done in this analysis for all backgrounds involving prompt lep-
 1131 tons: $t\bar{t}W$, $t\bar{t}Z$, $t\bar{t}H$, WZ , ZZ , $W^\pm W^\pm qq$, $t\bar{t}t\bar{t}$, tZq , tZW , WWW , WWZ , WZZ ,
 1132 ZZZ .

1133 Reducible backgrounds, on the other hand, are not well predicted by simulation,
 1134 and are estimated using data-driven methods. In the case of non-prompt leptons, a
 1135 fake rate method is used, where the contribution to the final selection is estimated by
 1136 extrapolating from a sideband (or “application region”) with a looser lepton definition
 1137 (the fakeable object definitions in Tabs. 4.7 and 4.8) to the signal selection. The tight-
 1138 to-loose ratios (or “fake rates”) are measured in several background dominated data
 1139 events with dedicated triggers, subtracting the residual prompt lepton contribution
 1140 using MC. Non-prompt leptons in our signal regions are predominantly produced in $t\bar{t}$
 1141 events, with a much smaller contribution, from Drell–Yan production. The systematic
 1142 uncertainty on the normalization of the non-prompt background estimation is on the

order of 50%, and thereby one of the dominant limitations on the performance of multilepton analyses in general and this analysis in particular. It consists of several individual sources, such as the result of closure tests of the method using simulated events, limited statistics in the data control regions due to necessary prescaling of lepton triggers, and the uncertainty in the subtraction of residual prompt leptons from the control region.

The fake background where the leptons pass the looser selection are weighted according to how many of them fail the tight criteria. Events with a single failing lepton are weighted with the factor $f/(1-f)$ for the estimate to the tight selection region, where f is the fake rate. Events with two failing leptons are given the negative weight $-f_i f_j / (1-f_i)(1-f_j)$, and for three leptons the weight is positive and equal to the product of $f/(1-f)$ factor evaluated for each failing lepton.

Figures 4.2 show the distributions of some relevant kinematic variables, normalized to the cross section of the respective processes and to the integrated luminosity.

4.5 Signal discrimination

The tHq signal is separated from the main backgrounds using a boosted decision tree (BDT) classifier, trained on simulated signal and background events. A set of discriminating variables are given as input to the BDT which produces a output distribution maximizing the discrimination power. Table 4.9 lists the input variables used while Figures 4.3 show their distributions for the relevant signal and background samples, for the three lepton channel. Two BDT classifiers are trained for the two main backgrounds expected in the analysis: events with prompt leptons from $t\bar{t}W$ and $t\bar{t}Z$ (also referred to as $t\bar{t}V$), and events with non-prompt leptons from $t\bar{t}$. The datasets used in the training are the tHq signal (see Tab. 4.1), and LO MADGRAPH samples

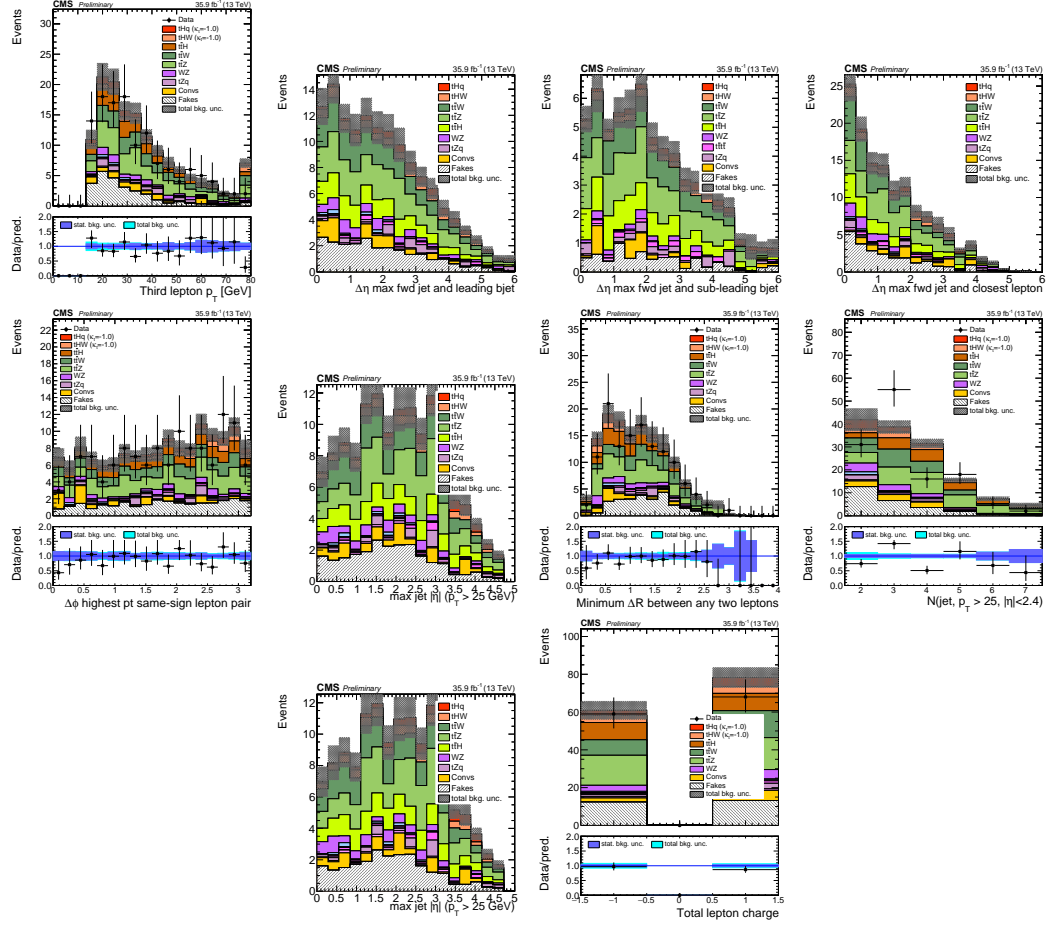


Figure 4.2: Distributions of input variables to the BDT for signal discrimination, three lepton channel, normalized to their cross section and to 35.9fb^{-1} .

of $t\bar{t}W$ and $t\bar{t}Z$, in an admixture proportional to their respective cross sections (see Tab. 4.4).

The MVA analysis consist of two stages: first a “training” where the MVA method is trained to discriminate between simulated signal and background events, then a “test” stage where the trained algorithm is used to classify different events from the samples. The sample is obtained from a pre-selection (see Tab. ?? with pre-selection cuts). Figures 4.4 show the input variables distributions as seen by the MVA algorithm. Note that in contrast to the distributions in Fig. 4.3 only the main backgrounds ($t\bar{t}$ from simulation, $t\bar{t}V$) are included.

Variable name	Description
nJet25	Number of jets with $p_T > 25$ GeV, $ \eta < 2.4$
MaxEtaJet25	Maximum $ \eta $ of any (non-CSV-loose) jet with $p_T > 25$ GeV
totCharge	Sum of lepton charges
nJetEta1	Number of jets with $ \eta > 1.0$, non-CSV-loose
detaFwdJetBJet	$\Delta\eta$ between forward light jet and hardest CSV loose jet
detaFwdJet2BJet	$\Delta\eta$ between forward light jet and second hardest CSV loose jet (defaults to -1 in events with only one CSV loose jet)
detaFwdJetClosestLep	$\Delta\eta$ between forward light jet and closest lepton
dphiHighestPtSSPair	$\Delta\phi$ of highest p_T same-sign lepton pair
minDRll	minimum ΔR between any two leptons
Lep3Pt/Lep2Pt	p_T of the 3 rd lepton (2 nd for ss2l)

Table 4.9: MVA input discriminating variables

1176 Note that splitting the training in two groups reveals that some variables show
 1177 opposite behavior for the two background sources; potentially screening the discrimi-
 1178 nation power if they were to be used in a single discriminant. For some other variables
 1179 the distributions are similar in both background cases.

1180 From table 4.9, it is clear that the input variables are correlated to some extend.
 1181 These correlations play an important role for some MVA methods like the Fisher
 1182 discriminant method in which the first step consist of performing a linear transfor-
 1183 mation to an phase space where the correlations between variables are removed. In
 1184 case a boosted decision tree (BDT) method however, correlations do not affect the
 1185 performance. Figure 4.6 show the linear correlation coefficients for signal and back-
 1186 ground for the two training cases (the signal values are identical by construction). As
 1187 expected, strong correlations appears for variables related to the forward jet activity.
 1188 Same trend is seen in case of the same sign dilepton channel in Figure ??.

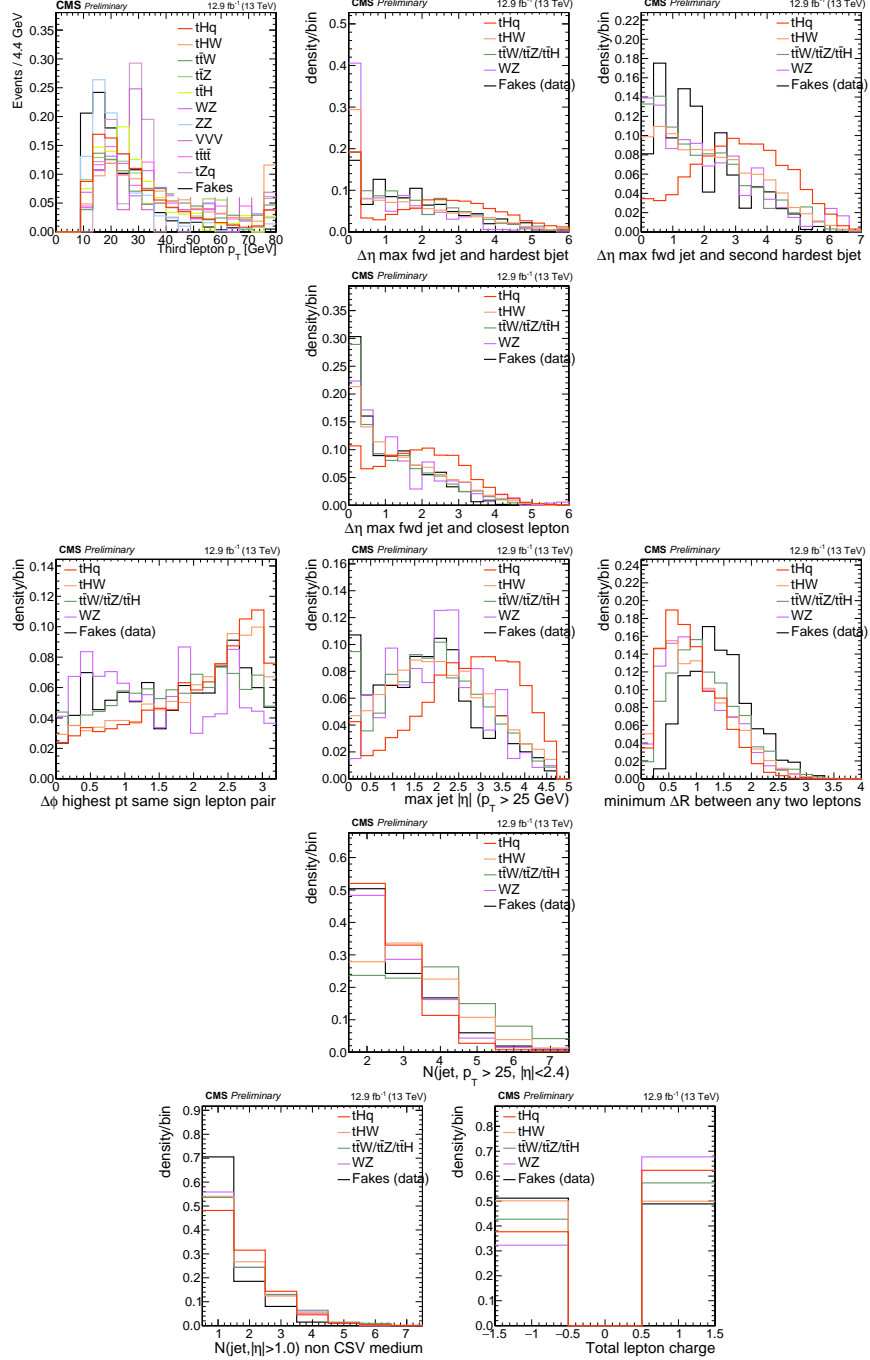


Figure 4.3: Distributions of input variables to the BDT for signal discrimination, three lepton channel.

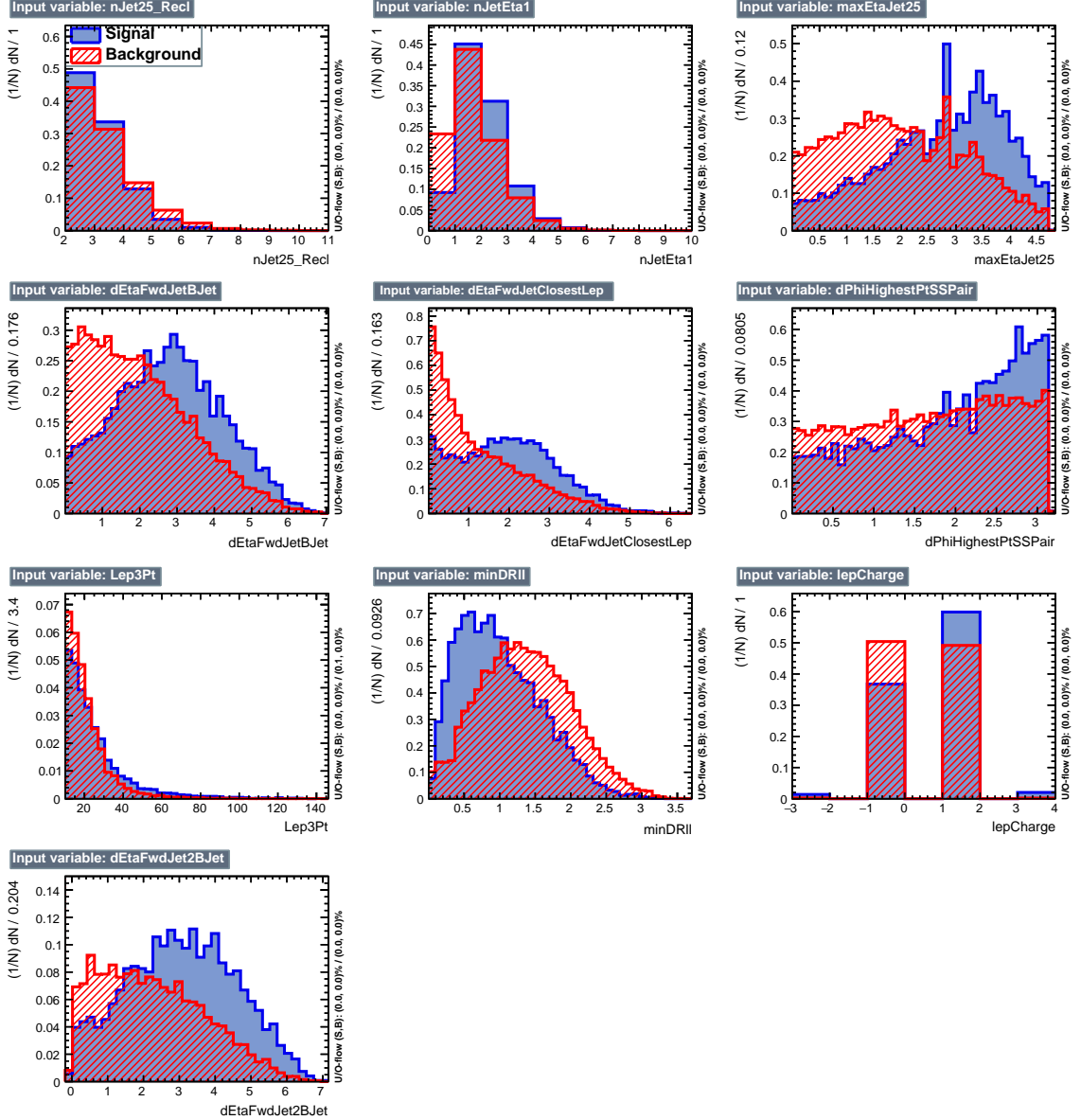


Figure 4.4: BDT inputs as seen by TMVA (signal, in blue, is tHq , background, in red, is $t\bar{t}$) for the three lepton channel, discriminated against $t\bar{t}$ (fakes) background.

1189 4.5.1 Classifiers response

1190 Several MVA algorithms were evaluated to determine the most appropriate method
 1191 for this analysis. The plots in Fig. 4.7 (top) show the background rejection as a
 1192 function of the signal efficiency for $t\bar{t}$ and $t\bar{t}V$ trainings (ROC curves) for the different

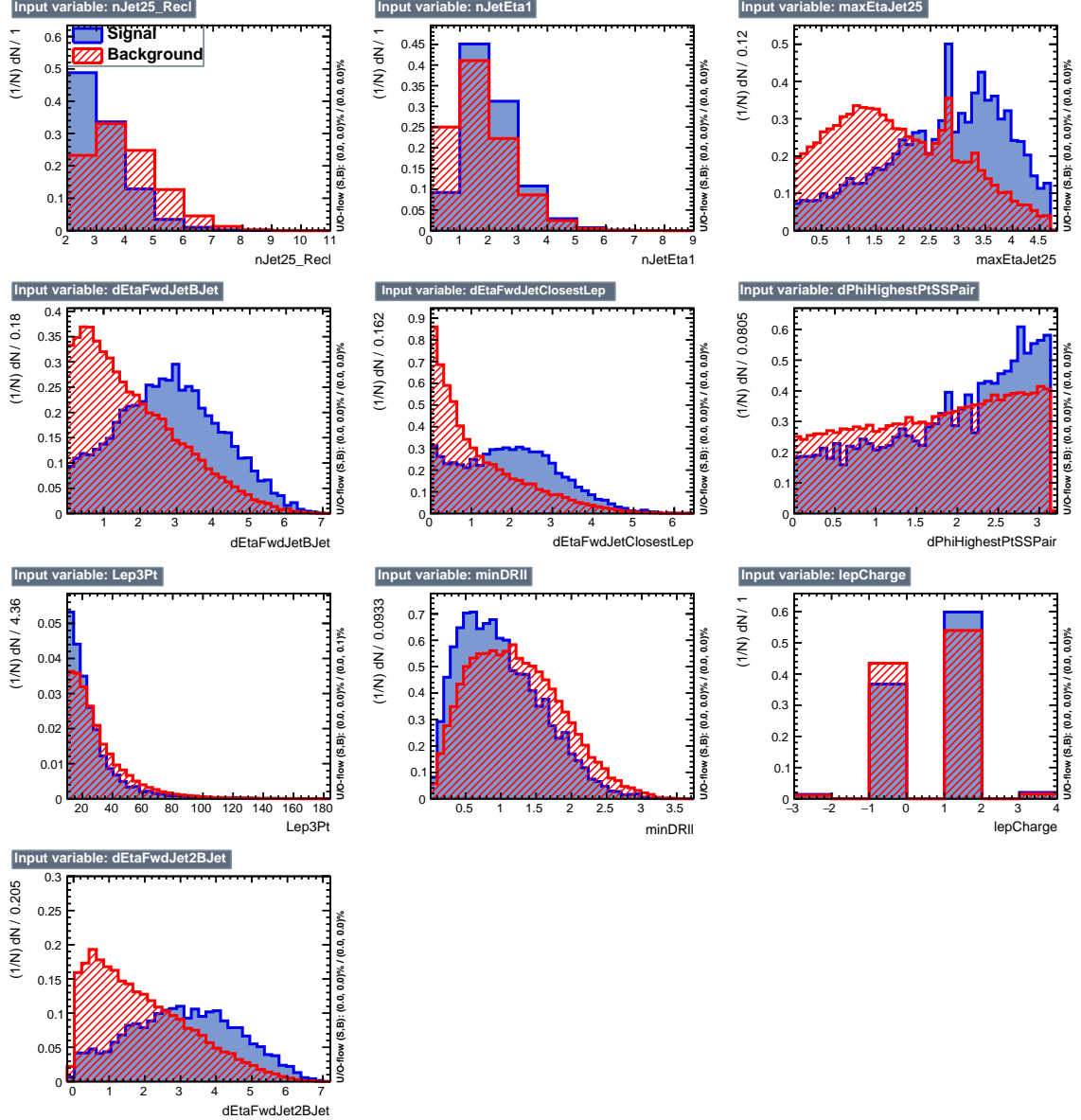


Figure 4.5: BDT inputs as seen by TMVA (signal, in blue, is tHq , background, in red, is $t\bar{t}W+t\bar{t}Z$) for the three lepton channel, discriminated against $t\bar{t}V$ background.

algorithms that were evaluated.

In both cases the gradient boosted decision tree (“BDTA_GRAD”) classifier offers the best results, followed by an adaptive BDT classifier (“BDTA”). The BDTA_GRAD classifier output distributions for signal and backgrounds are shown on the bottom of Fig. 4.7. As expected, a good discrimination power is obtained using default discrim-

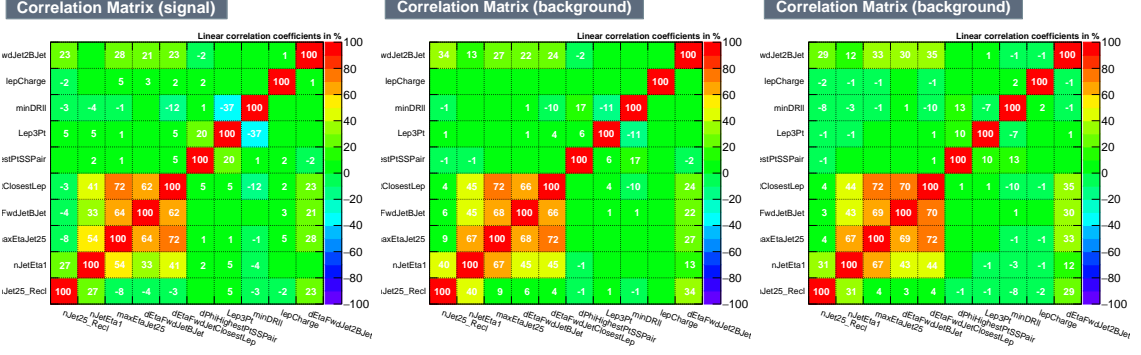


Figure 4.6: Signal (left), $t\bar{t}$ background (middle), and $t\bar{t}V$ background (right.) correlation matrices for the input variables in the TMVA analysis for the three lepton channel.

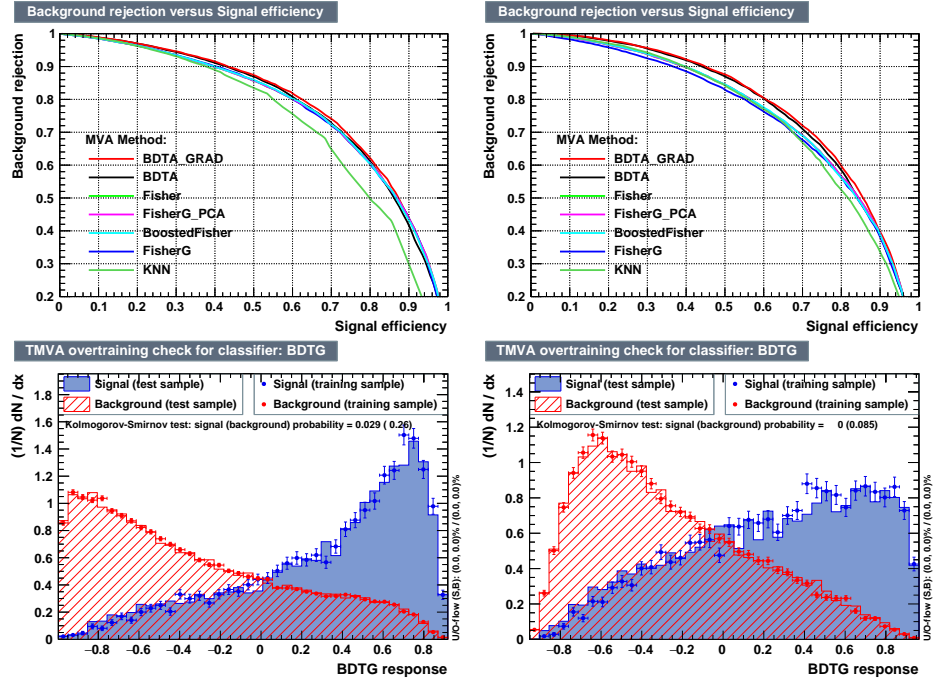


Figure 4.7: Top: background rejection vs signal efficiency (ROC curves) for various MVA classifiers (top) in the three lepton channel against $t\bar{t}V$ (left) and $t\bar{t}$ (right). Bottom: classifier output distributions for the gradient boosted decision trees, for training against $t\bar{t}V$ (left) and against $t\bar{t}$ (right).

1198 inator parameter values, with minimal overtraining. TMVA provides a ranking of the
 1199 input variables by their importance in the classification process, shown in Tab. 4.10.
 1200 The TMVA settings used in the BDT training are shown in Tab. 4.11.

ttbar training			ttV training		
Rank	Variable	Importance	Variable	Importance	Importance
1	minDRll	1.329e-01	dEtaFwdJetBJet	1.264e-01	
2	dEtaFwdJetClosestLep	1.294e-01	Lep3Pt	1.224e-01	
3	dEtaFwdJetBJet	1.209e-01	maxEtaJet25	1.221e-01	
4	dPhiHighestPtSSPair	1.192e-01	dEtaFwdJet2BJet	1.204e-01	
5	Lep3Pt	1.158e-01	dEtaFwdJetClosestLep	1.177e-01	
6	maxEtaJet25	1.121e-01	minDRll	1.143e-01	
7	dEtaFwdJet2BJet	9.363e-02	dPhiHighestPtSSPair	9.777e-02	
8	nJetEta1	6.730e-02	nJet25_Recl	9.034e-02	
9	nJet25_Recl	6.178e-02	nJetEta1	4.749e-02	
10	lepCharge	4.701e-02	lepCharge	4.116e-02	

Table 4.10: TMVA input variables ranking for BDTA_GRAD method for the trainings in the three lepton channel. For both trainings the rankings show almost the same 5 variables in the first places.

```
TMVA.Types.kBDT
NTrees=800
BoostType=Grad
Shrinkage=0.10
!UseBaggedGrad
nCuts=50
MaxDepth=3
NegWeightTreatment=PairNegWeightsGlobal
CreateMVApdfs
```

Table 4.11: TMVA configuration used in the BDT training.

1201 4.6 Additional discriminating variables

1202 Two additional discriminating variables were tested considering the fact that the
 1203 forward jet in the background could come from the pileup; since we have a real
 1204 forward jet in the signal, it could give some improvement in the discriminating power.
 1205 The additional variables describe the forward jet momentum (fwdJetPt25) and the
 1206 forward jet identification(fwdJetPUID). Distributions for these variables in the three
 1207 lepton channel are shown in the figure 4.8. The forward jet identification distribution
 1208 show that for both, signal and background, jets are mostly real jets.

1209 The testing was made including in the MVA input one variable at a time, so we

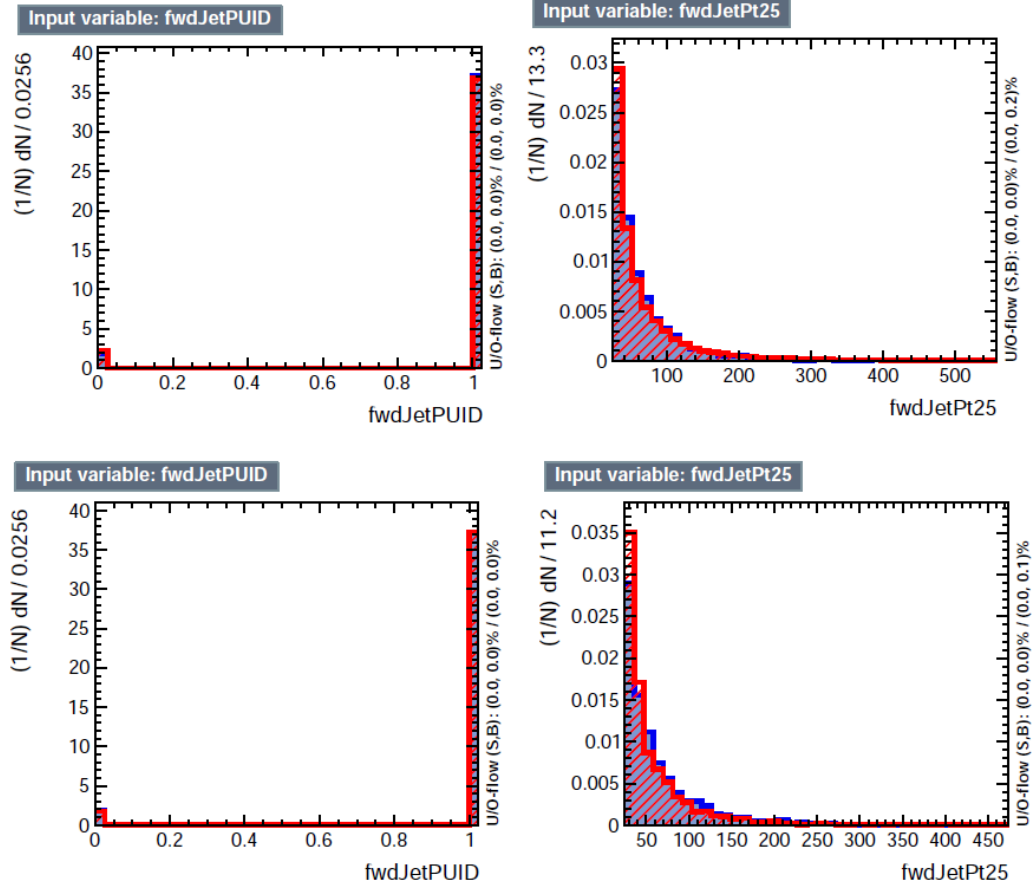


Figure 4.8: Additional discriminating variables distributions for ttV training (Top row) and tt training (bottom row) in the three lepton channel. The origin of the jets in the forward jet identification distribution is tagged as 0 for “pileup jets” while “real jets” are tagged as 1.

1210 can evaluate the discrimination power of each variable, and then both simultaneously.
 1211 fwdJetPUID was ranked in the last place in importance (11) in both training (ttV
 1212 and tt) while fwdJetPt25 was ranked 3 in the ttV training and 7 in the tt training.
 1213 When training using 12 variables, fwdJetPt25 was ranked 5 and 7 in the ttV and tt
 1214 trainings respectively, while fwdJetPUID was ranked 12 in both cases.

1215 The improvement in the discrimination performance provided by the additional
 1216 variables is about 1%, so it was decided not to include them in the procedure. Table
 1217 4.12 show the ROC-integral for all the testing cases we made.

ROC-integral	
base 10 var ttv	0.848
+ fwdJetPUID ttv	0.849
+ fwdJetPt25 ttv	0.856
12 var ttv	0.856
<hr/>	
base 10 var tt	0.777
+ fwdJetPUID tt	0.777
+ fwdJetPt25 tt	0.787
12 var	0.787

Table 4.12: ROC-integral for all the testing cases we made in the evaluation of the additional variables discriminating power. The improvement in the discrimination performance provided by the additional variables is about 1%

¹²¹⁸ **Chapter 5**

¹²¹⁹ **The CMS forward pixel detector**

¹²²⁰ **5.0.1 The phase 1 FPix upgrade**

¹²²¹ **5.0.2 FPix module production line**

¹²²² **5.0.3 The Gluing stage**

¹²²³ **5.0.4 The Encapsulation stage**

¹²²⁴ **5.0.5 The FPix module production yields**

1225 References

- 1226 [1] D.J. Griffiths, “Introduction to electrodynamics”. 4th ed. Pearson, (2013).
- 1227 [2] F. Mandl, G. Shaw. “Quantum field theory.” Chichester: Wiley (2009).
- 1228 [3] F. Halzen, and A.D. Martin, “Quarks and leptons: An introductory course in
1229 modern particle physics”. New York: Wiley, (1984) .
- 1230 [4] J.C. Maxwell. “A dynamical theory of the electromagnetic field”. Philosophical
1231 Transactions of the Royal Society of London. 155: 459â€¢512.(1865)
1232 doi:10.1098/rstl.1865.0008
- 1233 [5] M. Planck. “ÃIJber das Gesetz der Energieverteilung im Normalspektrum”.
1234 Annalen der Physik. 4 (3): 553.(1901).
- 1235 [6] A. Einstein “ÃIJber einen die Erzeugung und Verwandlung des Lichtes betref-
1236 fenden heuristischen Gesichtspunkt”. Annalen der Physik. 17 (6): 132â€¢148,
1237 (1905).
- 1238 [7] A. Einstein. “ÃIJber die von der molekularkinetischen Theorie der WÃdrme
1239 geforderte Bewegung von in ruhenden FlÃijssigkeiten suspendierten Teilchen”.
1240 Annalen der Physik. 17 (8): 549â€¢560, (1905).
- 1241 [8] A. Einstein. “Zur Elektrodynamik bewegter KÃürper”. Annalen der Physik. 17
1242 (10): 891â€¢921, (1905).

- 1243 [9] A. Einstein, "Ist die TrÄdgheit eines KÃürpers von seinem Energieinhalt ab-
 1244 hÃdngig?". Annalen der Physik. 18 (13): 639â€¢641, (1905).
- 1245 [10] B. P. Abbott et al. "Observation of Gravitational Waves from a Binary Black
 1246 Hole Merger". PRL 116, 061102 (2016).
- 1247 [11] J. Schwinger. "Quantum Electrodynamics. I. A Covariant Formulation". Phys-
 1248 ical Review. 74 (10): 1439â€¢61, (1948).
- 1249 [12] R. P. Feynman. "Spaceâ€¢Time Approach to Quantum Electrodynamics".
 1250 Physical Review. 76 (6): 769â€¢89, (1949).
- 1251 [13] S. Tomonaga. "On a Relativistically Invariant Formulation of the Quantum
 1252 Theory of Wave Fields". Progress of Theoretical Physics. 1 (2): 27â€¢42, (1946).
- 1253 [14] S.L. Glashow. "Partial symmetries of weak interactions", Nucl. Phys. 22 579-
 1254 588, (1961).
- 1255 [15] A. Salam, J.C. Ward. "Electromagnetic and weak interactions", Physics Letters
 1256 13 168-171, (1964).
- 1257 [16] S. Weinberg, "A model of leptons", Physical Review Letters, vol. 19, no. 21, p.
 1258 1264, (1967).
- 1259 [17] E. Noether, "Invariante Variationsprobleme", Nachrichten von der Gesellschaft
 1260 der Wissenschaften zu GÃüttingen, mathematisch-physikalische Klasse, vol.
 1261 1918, pp. 235â€¢257, (1918).
- 1262 [18] File:Standard_Model_of_Elementary_Particle_dark.svg. (2017, June 12)
 1263 Wikimedia Commons, the free media repository. Retrieved November 27,
 1264 2017 from <https://www.collegiate-advanced-electricity.com/single-post/2017/04/10/The-Standard-Model-of-Particle-Physics>.

- 1266 [19] M. Goldhaber, L. Grodzins, A.W. Sunyar “Helicity of Neutrinos”, Phys. Rev.
 1267 109, 1015 (1958).
- 1268 [20] Palanque-Delabrouille N et al. “Neutrino masses and cosmology with Lyman-
 1269 alpha forest power spectrum”, JCAP 11 011 (2015).
- 1270 [21] C. Patrignani et al. (Particle Data Group), Chin. Phys. C, 40, 100001 (2016)
 1271 and 2017 update.
- 1272 [22] M. Gell-Mann. “A Schematic Model of Baryons and Mesons”. Physics Letters.
 1273 8 (3): 214–215 (1964).
- 1274 [23] G. Zweig. “An SU(3) Model for Strong Interaction Symmetry and its Breaking”
 1275 (PDF). CERN Report No.8182/TH.401 (1964).
- 1276 [24] G. Zweig. “An SU(3) Model for Strong Interaction Symmetry and its Breaking:
 1277 II” (PDF). CERN Report No.8419/TH.412(1964).
- 1278 [25] M. Gell-Mann. “The Interpretation of the New Particles as Displaced Charged
 1279 Multiplets”. Il Nuovo Cimento 4: 848. (1956).
- 1280 [26] T. Nakano, K. Nishijima. “Charge Independence for V-particles”. Progress of
 1281 Theoretical Physics 10 (5): 581-582. (1953).
- 1282 [27] N. Cabibbo, “Unitary symmetry and leptonic decays” Physical Review Letters,
 1283 vol. 10, no. 12, p. 531, (1963).
- 1284 [28] M.Kobayashi, T.Maskawa, “CP-violation in the renormalizable theory of weak
 1285 interaction,” Progress of Theoretical Physics, vol. 49, no. 2, pp. 652-657, (1973).
- 1286 [29] File:Weak Decay (flipped).svg. (2017, June 12). Wikimedia Com-
 1287 mons, the free media repository. Retrieved November 27, 2017

- 1288 from `https : //commons.wikimedia.org/w/index.php?title = File :`
 1289 `Weak_Decay_(flipped).svg&oldid = 247498592.`
- 1290 [30] Georgia Tech University. Coupling Constants for the Fundamental
 1291 Forces(2005). Retrieved January 10, 2018, from `http://hyperphysics.phy –`
 1292 `astr.gsu.edu/hbase/Forces/couple.html#c2`
- 1293 [31] M. Strassler. (May 31, 2013).The Strengths of the Known Forces. Retrieved
 1294 January 10, 2018, from `https://profmattstrassler.com/articles – and –`
 1295 `posts/particle – physics – basics/the – known – forces – of – nature/the –`
 1296 `strength – of – the – known – forces/`
- 1297 [32] M. Peskin, D. Schroeder, “An introduction to quantum field theory”. Perseus
 1298 Books Publishing L.L.C., (1995).
- 1299 [33] A. Pich. “The Standard Model of Electroweak Interactions”
 1300 `https://arxiv.org/abs/1201.0537`
- 1301 [34] F.Bellaiche. (2012, 2 September). “What’s this Higgs boson anyway?”. Retrieved
 1302 from: `https://www.quantum-bits.org/?p=233`
- 1303 [35] M. Endres et al. Nature 487, 454-458 (2012) doi:10.1038/nature11255
- 1304 [36] F. Englert, R. Brout. “Broken Symmetry and the Mass of Gauge Vec-
 1305 tor Mesons”. Physical Review Letters. 13 (9): 321–323.(1964) Bib-
 1306 code:1964PhRvL..13..321E. doi:10.1103/PhysRevLett.13.321
- 1307 [37] P.Higgs. “Broken Symmetries and the Masses of Gauge Bosons”. Physical
 1308 Review Letters. 13 (16): 508–509,(1964). Bibcode:1964PhRvL..13..508H.
 1309 doi:10.1103/PhysRevLett.13.508.

- 1310 [38] G.Guralnik, C.R. Hagen and T.W.B. Kibble. “Global Conservation Laws and
 1311 Massless Particles”. Physical Review Letters. 13 (20): 585–587, (1964). Bib-
 1312 code:1964PhRvL..13..585G. doi:10.1103/PhysRevLett.13.585.
- 1313 [39] CMS collaboration. “Observation of a new boson at a mass of 125
 1314 GeV with the CMS experiment at the LHC”. Physics Letters B.
 1315 716 (1): 30–61 (2012). arXiv:1207.7235. Bibcode:2012PhLB..716...30C.
 1316 doi:10.1016/j.physletb.2012.08.021
- 1317 [40] ATLAS collaboration. “Observation of a New Particle in the Search for the Stan-
 1318 dard Model Higgs Boson with the ATLAS Detector at the LHC”. Physics Let-
 1319 ters B. 716 (1): 1–29(2012). arXiv:1207.7214 Bibcode:2012PhLB..716....1A.
 1320 doi:10.1016/j.physletb.2012.08.020.
- 1321 [41] ATLAS collaboration; CMS collaboration (26 March 2015). “Combined
 1322 Measurement of the Higgs Boson Mass in pp Collisions at $\sqrt{s}=7$ and
 1323 8 TeV with the ATLAS and CMS Experiments”. Physical Review Let-
 1324 ters. 114 (19): 191803. arXiv:1503.07589. Bibcode:2015PhRvL.114s1803A.
 1325 doi:10.1103/PhysRevLett.114.191803.
- 1326 [42] CMS Collaboration, “SM Higgs Branching Ratios and To-
 1327 tal Decay Widths (up-date in CERN Report4 2016)”.
 1328 <https://twiki.cern.ch/twiki/bin/view/LHCPhysics/CERNYellowReportPageBR>, last accessed on 17.12.2017.
- 1330 [43] R.Grant V. “Determination of Higgs branching ratios in $H \rightarrow W^+W^- \rightarrow l^+l^- jj$ and $H \rightarrow ZZ \rightarrow l^+l^- jj$ channels”. Physics Department, Uni-
 1331 versity of Tennessee (Dated: October 31, 2012). Retrieved from
 1332 <http://aesop.phys.utk.edu/ph611/2012/projects/Riley.pdf>

- 1334 [44] LHC Higgs Cross Section Working Group, Denner, A., Heinemeyer, S. et al.
 1335 “Standard model Higgs-boson branching ratios with uncertainties”. Eur. Phys.
 1336 J. C (2011) 71: 1753. <https://doi.org/10.1140/epjc/s10052-011-1753-8>
- 1337 [45] LHC InternationalMasterclasses“When protons collide”. Retrieved from
 1338 http://atlas.physicsmasterclasses.org/en/zpath_protoncollisions.htm
- 1339 [46] F. Maltoni, K. Paul, T. Stelzer, and S. Willenbrock, “Associated production
 1340 of Higgs and single top at hadron colliders”, Phys.Rev. D64 (2001) 094023,
 1341 [hep-ph/0106293].
- 1342 [47] S. Biswas, E. Gabrielli, F. Margaroli, and B. Mele, “Direct constraints on the
 1343 top-Higgs coupling from the 8 TeV LHC data,” Journal of High Energy Physics,
 1344 vol. 07, p. 073, (2013).
- 1345 [48] M. Farina, C. Grojean, F. Maltoni, E. Salvioni, and A. Thamm, “Lifting de-
 1346 generacies in Higgs couplings using single top production in association with a
 1347 Higgs boson,” Journal of High Energy Physics, vol. 05, p. 022, (2013).
- 1348 [49] T.M. Tait and C.-P. Yuan, “Single top quark production as a window to physics
 1349 beyond the standard model”, Phys. Rev. D 63 (2000) 014018 [hep-ph/0007298].
- 1350 [50] F. Demartin, F. Maltoni, K. Mawatari, and M. Zaro, “Higgs production in
 1351 association with a single top quark at the LHC,” European Physical Journal C,
 1352 vol. 75, p. 267, (2015).
- 1353 [51] CMS Collaboration, “Modelling of the single top-quark pro-
 1354 duction in association with the Higgs boson at 13 TeV.”
 1355 <https://twiki.cern.ch/twiki/bin/viewauth/CMS/SingleTopHiggsGeneration13TeV>,
 1356 last accessed on 16.01.2018.

- 1357 [52] CMS Collaboration, “SM Higgs production cross sections at $\sqrt{s} = 13$ TeV.”
 1358 <https://twiki.cern.ch/twiki/bin/view/LHCPhysics/CERNYellowReportPageAt13TeV>,
 1359 last accessed on 16.01.2018.
- 1360 [53] S. Dawson, The effective W approximation, Nucl. Phys. B 249 (1985) 42.
- 1361 [54] S. Biswas, E. Gabrielli and B. Mele, JHEP 1301 (2013) 088 [arXiv:1211.0499
 1362 [hep-ph]].
- 1363 [55] F. Demartin, B. Maier, F. Maltoni, K. Mawatari, and M. Zaro, “tWH associated
 1364 production at the LHC”, European Physical Journal C, vol. 77, p. 34, (2017).
 1365 arXiv:1607.05862
- 1366 [56] LHC Higgs Cross Section Working Group, “Handbook of LHC Higgs Cross
 1367 Sections: 4.Deciphering the Nature of the Higgs Sector”, arXiv:1610.07922.
- 1368 [57] J. Ellis, D. S. Hwang, K. Sakurai, and M. Takeuchi.“Disentangling Higgs-Top
 1369 Couplings in Associated Production”, JHEP 1404 (2014) 004, [arXiv:1312.5736].
- 1370 [58] CMS Collaboration, V. Khachatryan et al., “Precise determination of the mass
 1371 of the Higgs boson and tests of compatibility of its couplings with the standard
 1372 model predictions using proton collisions at 7 and 8 TeV,” arXiv:1412.8662.
- 1373 [59] ATLAS Collaboration, G. Aad et al., “Updated coupling measurements of the
 1374 Higgs boson with the ATLAS detector using up to 25 fb^{-1} of proton-proton
 1375 collision data”, ATLAS-CONF-2014-009.
- 1376 [60] ATLAS and CMS Collaborations, “Measurements of the Higgs boson produc-
 1377 tion and decay rates and constraints on its couplings from a combined ATLAS
 1378 and CMS analysis of the LHC pp collision data at $\sqrt{s} = 7$ and 8 TeV,” (2016).
 1379 CERN-EP-2016-100, ATLAS-HIGG-2015-07, CMS-HIG-15-002.

- 1380 [61] J.-L. Caron , “Layout of the LEP tunnel including future LHC infrastructures.”,
 1381 (Nov, 1993). A C Collection. Legacy of AC. Pictures from 1992 to 2002. Re-
 1382 trieved from <https://cds.cern.ch/record/841542>
- 1383 [62] CMS Collaboration, “Search for the associated production of a Higgs boson
 1384 with a single top quark in proton-proton collisions at $\sqrt{s} = 8$ TeV”, JHEP 06
 1385 (2016) 177,doi:10.1007/JHEP06(2016)177, arXiv:1509.08159.
- 1386 [63] B. Stieger, C. Jorda Lope et al., “Search for Associated Production of a Single
 1387 Top Quark and a Higgs Boson in Leptonic Channels”, CMS Analysis Note CMS
 1388 AN-14-140, 2014.
- 1389 [64] M. Peruzzi, C. Mueller, B. Stieger et al., “Search for ttH in multilepton final
 1390 states at $\sqrt{s} = 13$ TeV”, CMS Analysis Note CMS AN-16-211, 2016.
- 1391 [65] CMS Collaboration, “Search for H to bbar in association with a single top quark
 1392 as a test of Higgs boson couplings at $\sqrt{s} = 13$ TeV”, CMS Physics Analysis
 1393 Summary CMS-PAS-HIG-16-019, 2016.
- 1394 [66] B. Maier, “SingleTopHiggProduction13TeV”, February, 2016.
 1395 <https://twiki.cern.ch/twiki/bin/viewauth/CMS/SingleTopHiggsGeneration13TeV>.
- 1396 [67] M. Peruzzi, F. Romeo, B. Stieger et al., “Search for ttH in multilepton final1
 1397 states at $\sqrt{s} = 13$ TeV”, CMS Analysis Note CMS AN-17-029, 2017.
- 1398 [68] B. WG, “BtagRecommendation80XReReco”, February, 2017.
 1399 <https://twiki.cern.ch/twiki/bin/view/CMS/BtagRecommendation80XReReco>.